Bookshelf Kinematics and the Effect of Dilatation on Fault Zone Inelastic Deformation: Examples from Optical Image Correlation Measurements of the 2019 Ridgecrest Earthquake Sequence

Christopher Milliner[1,2*], Andrea Donnellan[1], Saif Aati[2], Jean-Philippe Avouac[2], Robert Zinke[1], James F. Dolan[3], Kang Wang[4], Roland Bürgmann[4]

[1] *Jet Propulsion Laboratory, California Institute of Technology, Pasadena, CA*
[2] *California Institute of Technology, Pasadena, CA*
[3] *University of Southern California, Los Angeles, CA*
[4] *University of California, Berkeley, Berkeley, CA*
**corresponding author. milliner@caltech.edu*

This manuscript has been submitted for publication in Journal of Geophysical Research:Solid Earth. Please note that the peer-review is in progress, and subsequent versions of this manuscript may have different content. If accepted, the final version of this manuscript will be available via the ' Peer-reviewed publication DOI' link on the EarthArxiv webpage.

Bookshelf Kinematics and the Effect of Dilatation on Fault Zone Inelastic Deformation: Examples from Optical Image Correlation Measurements of the 2019 Ridgecrest Earthquake Sequence

Christopher Milliner[1,2*], Andrea Donnellan[1], Saif Aati[2], Jean-Philippe Avouac[2], Robert Zinke[1], James F. Dolan[3], Kang Wang[4], Roland Bürgmann[4]

[1] Jet Propulsion Laboratory, California Institute of Technology, Pasadena, CA
[2] California Institute of Technology, Pasadena, CA
[3] University of Southern California, Los Angeles, CA
[4] University of California, Berkeley, Berkeley, CA
**corresponding author*

Key Points

- We resolve finite strain, rotation and dilatation, finding wider fault zones along transtensional bends due to increasing extension
- The foreshock has larger off-fault strain (56%) than the mainshock (34%) suggesting it is less mature, and why its slip deficit is larger
- Large rotations beyond fault tips explain why conjugate faults do not intersect and that cross-faulting results from bookshelf kinematics

Abstract

The 2019 Ridgecrest earthquake sequence initiated on July 4th with a series of foreshocks, including a M_w 6.4 event, that culminated a day later with the M_w 7.1 mainshock and resulted in rupture of a set of cross-faults. Here we use sub-pixel correlation of optical satellite imagery to measure the displacement, finite strain and rotation of the near-field coseismic deformation to understand the kinematics of strain release along the surface ruptures. We find the average off-fault deformation along the mainshock rupture is 34% and is significantly higher along the foreshock rupture (56%) suggesting it is a less structurally developed fault system. Measurements of the 2D dilatational strain along the mainshock rupture show a dependency of the width of inelastic strain with the degree of fault extension and contraction, indicating wider fault zones under extension than under shear. Measurements of the vorticity along the main, dextral rupture show that conjugate sinistral faults are embedded within zones of large clockwise rotations caused by the transition of strain beyond the tips of dextral faults leading to bookshelf kinematics. These rotations and bookshelf slip can explain why faults of different shear senses do not intersect one another and the occurrence of pervasive and mechanically unfavorable cross-faulting in this region. Understanding the causes for the variation of fault-zone widths along surface ruptures has importance for reducing the epistemic uncertainty of probabilistic models of distributed rupture that will in turn provide more precise estimates of the hazard distributed rupture poses to nearby infrastructure.

Keywords: Ridgecrest, inelastic, off-fault deformation, finite strain, rotation, dilatation, distributed rupture

1.1 Introduction

The 2019 Ridgecrest earthquake sequence initiated on July 4th with a series of foreshocks that included a M_w 6.4 event and culminated 34 hours later with a M_w 7.1 mainshock event. This sequence was also notable in that it resulted in rupture of a set of more than 20 cross-faults (Brandenberg et al., 2020; Ross et al., 2019; Xu et al., 2020). The earthquake sequence occurred within the northern region of the Eastern California Shear Zone (ECSZ), a 150-km-wide zone of NW-trending dextral shear that accommodates up to ~20% of the North America-Pacific plate boundary motion (McClusky et al., 2001; Rockwell et al., 2000). Seismic and geodetic inversions show the M_w 6.4 event likely ruptured multiple fault segments, where it initiated on a short NW-trending, dextral fault, and then propagated to the southwest along a series of parallel NE-trending sinistral faults for 16 km (Liu et al., 2019; Ross et al., 2019; Chen et al., 2020; Goldberg et al., 2020; Wang et al., 2020). On July 5^{th}, 34 hours after the foreshock, the M_w 7.1 mainshock initiated ~15 km to the north, from where it propagated bilaterally at a relatively slow velocity of ~2 km/s along a NW-trending set of dextral faults for ~45 km. The mainshock rupture terminated at its northern extent within the Coso volcanic field and at its southern extent ~5 km from the Garlock fault, where it was found to have triggered creep at the surface along parts of the Garlock fault and a small cluster of seismicity (Barnhart et al., 2019; Ross et al., 2019). The Ridgecrest sequence is also notable in that it occurred within a region of similar sized events, including the M_w ~7.5 1872 Owens Valley earthquake located ~45 km to the north, and the 1992 M_w 7.3 Landers and 1999 M_w 7.1 Hector Mine earthquakes ~110 km to the south.

Here we use optical image correlation of satellite data to measure the near-field surface deformation patterns and study the kinematics of finite fault strain release along the Ridgecrest surface ruptures. Documenting coseismic surface strain is important as we describe in section 1.2, as it can alter the fault zone mechanical properties which are relevant to understanding earthquake dynamics and is an important input for constraining probabilistic models of distributed fault rupture hazard (e.g., Petersen et al., 2011). Here, we assess whether fault zones are wider and the strain distribution different under tension, and assess the effects of rotations adjacent to faults that may explain the occurrence of mechanically unfavorable cross-faulting. We also use our observations of surface strain to shed light on the regional scale tectonic questions of the Eastern California Shear Zone (ECSZ) and Garlock fault which we describe in the second section below.

1.2 Significance of distributed inelastic strain

Distributed inelastic strain is accommodated via a range of mechanisms across fault zones, including secondary fracturing, pervasive continuous shear and rotations (Shelef and Oskin, 2010). These act to alter the mechanical properties of the fault-zone material which can affect a range of earthquake processes including the attenuation of seismic waves (Mitchell, 1995), dissipation of rupture energy and velocity (Sammis et al., 2010; Dunham et al., 2011; Gabriel et al., 2013; Thomas and Bhat, 2018; Bao et al., 2019), and the ability of ruptures to fully reach the surface (Kaneko and Fialko, 2011). Therefore, understanding what controls the variation of the magnitude, width and spatial decay of inelastic strain across fault zones has importance for seismic hazard, both for accurately estimating the probability of seismic shaking and distributed fault displacement (McGuire, 1995; Petersen et al., 2011). It is also important for accurately estimating geologic fault slip rates that are susceptible to underestimating the long-term displacement when restoring offset geomorphic features across fault zones (Dolan and Haravitch, 2014; Scharer et al., 2014).

Measurements of off-fault deformation (OFD) from field survey mapping and remote-based methods (e.g. lidar differencing and optical image correlation) of surface ruptures have shown that the sediment thickness, type of near-surface material and fault dip have an important effect on the amounts of off-fault distributed inelastic deformation (Rockwell et al., 2002; Dolan and Haravitch, 2014; Zinke et al., 2014; Gold et al., 2015; Teran et al., 2015; Milliner et al., 2015; 2016; Scott et al., 2018; Zhou et al., 2018). However, how the distribution and magnitude of inelastic strain varies in regions where the fault experiences fault-normal contraction and extension is less well understood. This is largely due to the difficulty of measuring the fault-perpendicular component of displacement in the field and the challenge of accurately estimating strain from geodetic displacement measurements which requires sufficiently high-resolution sampling and low noise when calculating the spatial derivatives. Here we analyze the surface deformation due to the 2019 Ridgecrest earthquakes for which such measurements exist. Specifically, we use these data to evaluate the sensitivity of the width and spatial attenuation of inelastic strain across the surface rupture to the amount of extension and contraction the fault zone experiences.

From our observations of the kinematics of surface strain we also seek to understand the widespread occurrence of orthogonal cross-faulting along the surface rupture. Cross-faulting occurred at almost all scales as shown by 100-m-long distributed fractures (Ponti et al., 2019; Xu et al., 2020), to the coseismic rupture strands involved directly in the foreshock-mainshock sequence and the distribution of aftershocks, which suggests cross-faulting is pervasive through the seismogenic crust and is not just a surficial feature (Ross et al., 2019). Similar cross-faulting rupture behavior has been observed during other large earthquakes (e.g., the 1987 Superstition Hills) and seems to be a common mode of strain release along the North American-Pacific plate boundary (Hudnut et al., 1989; Smith et al., 2020). Although the occurrence of faults with nearly orthogonal orientations is not uncommon, it is still poorly understood as the conventional Mohr-Coulomb faulting theory predicts that faults form at 30º from the direction of maximum compression and ~60º from one another (Anderson, 1951). Here we attempt to understand why faults may occur in these mechanically unfavorable orientations by assessing the near-field kinematics along the Ridgecrest surface rupture at various scales which relate to different evolutionary stages of fault development.

We note that in our study we refer to the inelastic strain that is distributed across the fault zone and adjacent to the primary fault strand as off-fault deformation (OFD) and not as fault damage. Damage has been detected following major surface rupturing events by a decrease in the seismic velocity across the fault zone that is thought to occur by the generation of microcracks which reduces the rock's shear rigidity (Vidale and Li, 2003). Postseismically the seismic velocity of the damaged material has been found to recover and increase with time due to the closing and healing of microcracks, which indicates damage exhibits a time dependent behavior (Li et al., 2001). Damage can also be generated by the dynamic passing seismic waves with very little true shear strain in the form of shattered or "pulverized rocks" (Dor et al., 2006). In contrast the inelastic strain that we measure here is permanent, occurs at a much larger spatial and displacement scale (both > 10 cm's) than microcracking and results from both the quasi-static and dynamic stresses. This suggests that in some cases damage and off-fault deformation reflect rock failure associated with different processes and scales, and therefore here we do not use the two terms interchangeably.

1.3 Regional Tectonics and outstanding questions

Why the major faults in the ECSZ do not intersect or displace one another has been another long-standing issue because the kinematic evolution of fault junctions is not clear over long-term, geologic timescales. (Andrew and Walker, 2017; Frankel et al., 2008; Oskin and Iriondo, 2004; Oskin et al., 2008). For example, none of the major NW-trending dextral faults in the Mojave ECSZ (e.g., the Blackwater, Gravel Hills, North Lockhart and East Goldstone Lake faults) continue northward to intersect or displace the central Garlock fault. The same can also be found at the southern margin of the Mojave Desert for the sinistral Pinto Mountain fault near the southern termination of the 1992 Landers rupture (Sieh et al., 1993). Numerical modeling and long-term geologic structural evidence indicate that dextral strain likely transitions to distributed off-fault deformation beyond fault tips (Andrew and Walker, 2017; Herbert et al., 2014). Paleomagnetic studies in this region have provided constraint of the rotation of panels of crustal blocks associated with regional-scale bookshelf faulting, finding rotations of up to ~40° over the past ~10 Ma (Schermer et al. 1996; Miller and Yount, 2002). However, there are an insufficient number of paleomagnetic measurements that constrain the spatial distribution and magnitude of rotations beyond the tips of NW-trending dextral faults to understand how the long-term elastic strain is released at the junctures with conjugate sinistral faults. Here, we seek to provide measurements of coseismic finite strain and rotations along the Ridgecrest rupture to understand how dextral shear strain may transition to rotation beyond fault tips and whether this can explain why the major conjugate faults in this region do not physically connect.

To answer the questions outlined above we used optical image correlation to, i) measure the 2D dilatational, shear and rotational components of horizontal strain across different transpressional and transtensional geometrical bends of the surface rupture and ii) asses how the width of the fault zone varies according to the magnitude of extension and contraction it experiences. To provide more robust estimates of how the inelastic strain decays as a function of distance from the primary fault trace we developed a template-based stacking method that minimizes smoothing of displacement across the rupture, and we attempt to correct for the effect of smearing of the displacement signal caused by the convolution of the correlation window weighting function that arises during image matching. From the 2D displacement field we derive 2D finite strain maps and the infinitesimal vertical axis rotations to understand the kinematics of faulting along the rupture at the local and regional scale (10 and 100 km scale, respectively). We then use the strain and rotation maps to understand the mechanisms by which some faults in the ECSZ do not intersect or displace the Garlock fault, and the possible origin of cross-faulting and aftershock distributions given they are mechanically contradictory to conventional Mohr-Coulomb failure criteria.

2. Data & Methods

To measure the coseismic surface deformation we used subpixel image correlation of two optical SPOT-6 images that were acquired on September 15th, 2018 and July 24th, 2019 and therefore capture surface motion of both the foreshock and mainshock events. The SPOT images have a 60 km footprint and resolution of 1.5 m, with almost the same incidence angles (9.57º and 9.55º for the pre and post images respectively), which helps minimize topographic distortions that can arise from the parallax effect between different viewing geometries. To co-register, orthorectify and correlate the before and after images we used the COSI-Corr software (Leprince et al, 2007). The images are orthorectified using the satellite ancillary information which describes the exterior orientation (i.e., look angle, attitude and satellite position) and a 2 m pre-earthquake World-View DEM to correct for topographic distortions (Willis et al., 2019). The orthorectified and co-registered images were then correlated using COSI-Corr's phase correlator with a sliding window of 32×32 pixels and step of 4 pixels, producing a disparity map of the horizontal surface displacement at 6 m resolution (Figure 1, see supplements S1 for details on noise of the result and image artifacts).

To measure the total fault-parallel offset and decay of inelastic fault-parallel shear strain across the surface rupture first requires projecting the 2D displacement maps (Figure 1) into the local fault-parallel direction and then stacking over the profile swath width to minimize the effect of noise. Here we have developed a new stacking profile method that provides a more accurate estimate of the distribution of fault-parallel surface motion across the rupture over standard profile stacking approaches. Conventional stacking averages the fault-parallel motion along a constant direction over the profile swath width. However, this can be problematic as it ignores variations of the fault orientation within the profile swath that can lead to averaging of surface motion from either side of the fault, which results in smoothing of the displacement distribution, artificial widening of the fault zone and underestimation of the fault-parallel shear strains (see Figure S1 comparing conventional stacking versus our approach). To avoid this issue, we have developed a subpixel template alignment stacking method, which first aligns each individual profile line with subpixel precision prior to stacking. This is achieved by first creating a template from an initial stack that is then cross-correlated with each individual profile line (here we use an along-fault swath width of 138 m and across-fault profile length of 1-2 km, which involves 23 separate 'profile lines'). The optimal lateral shift to align each individual profile line is found with subpixel precision by determining the peak of an outlier-resistant cross correlation coefficient. Once the surface displacements are stacked with this approach, the total magnitude of the fault-parallel offset (i.e., the total amplitude of the discontinuity shown in Figure S2 and S13) is then estimated by inverting the fault-parallel displacements (*y*), which are a function of the distance across the profile (*x*), for the coefficients of a linear and error function (eq. 1 and 2).

$$y(x) = a + \frac{b}{2} \cdot \mathrm{erf}\left(\frac{x-c}{w_s\sqrt{2}}\right) + \varepsilon_{el} \cdot x \tag{1}$$

$$\mathrm{erf}(z) = \frac{2}{\sqrt{\pi}} \int_0^z e^{-t^2} dt\,, \quad z = \frac{x-c}{w_s\sqrt{2}} \tag{2}$$

The parameters, which include the intercept (*a*), total fault displacement (*b*), fault location (*c*), shear width (w_s) and slope (ε_{el}), are estimated using a non-linear regression as *c* and w_s are nonlinear in the model. The uncertainties for these are then estimated from the Jacobian, which contains the partial derivatives of the residuals with respect to the model parameters, that is used to calculate the model covariance matrix. The error function which characterizes the fault-parallel displacement across the fault zone implies that the distribution of fault-parallel inelastic shear strain follows a Gaussian distribution (i.e., the derivative of eq. 2). Therefore the variation of the fault-parallel shear strain (ε_{fp}, eq. [3]) across the fault zone can be expressed as the summation of the inelastic strain (ε_{inel}) and the fault-parallel elastic strain (ε_{el}, see Figure 13), which is given by the following relation using the chain rule,

$$\varepsilon_{fp}(x) = \frac{dy(x)}{dx} = \frac{b}{w_s\sqrt{2\pi}}\, e^{-z^2} + \varepsilon_{el} \tag{3}$$

$$\varepsilon_{fp}(x) = \varepsilon_{inel} + \varepsilon_{el} \tag{4}$$

In the displacement profiles (eq. 1), the elastic strain in the near-field is approximated by a linear trend which we find is reasonable given our profiles only sample the elastic dislocation signal within a short distance from the fault (≤1 km) compared to the length scale at which the elastic signal varies (which is ~*tan*(x) with a length scale proportional to the depth extent of fault slip Scholz [2019], which for Ridgecrest is 10-15 km and therefore a distance much longer than that of our profiles).

From the 2D displacement maps derived from the image correlation analysis we calculate the distribution of finite surface strain and local infinitesimal rotations. We first apply a non-local means filter to reduce the effects of noise and then calculate the spatial gradients of the displacement field and the finite strain tensor using a second-order accurate central difference approximation. Here we use the 2D displacement field $u_d(i,j)$ that is the output of the image correlation (Figure 1), where subscript d is the change of position between the pre and post-event satellite images in the east-west direction (denoted by subscript x) and north-south direction (denoted by subscript y), where i, j denote the indices of the displacement field in the x and y axes and Δx is the displacement map resolution (6 m). For example, the gradient of the east-west component of displacement in the x direction is calculated using the following finite difference approximation

$$\frac{\Delta u_x(i,j)}{\Delta x} = \frac{u_x(i+1,j) - u_x(i-1,j)}{2\Delta x} \tag{5}$$

Calculating the gradients of the displacement components (u_x, u_y) in the x, y directions gives the displacement gradient tensor, **D**,

$$\mathbf{D} = \begin{bmatrix} \left(\frac{\Delta u_x}{\Delta x}\right) & \left(\frac{\Delta u_x}{\Delta y}\right) \\ \left(\frac{\Delta u_y}{\Delta x}\right) & \left(\frac{\Delta u_y}{\Delta y}\right) \end{bmatrix} \tag{6}$$

To calculate strain we use the Lagrangian finite strain tensor (**E**) instead of the typical infinitesimal strain tensor because the condition of small strain is not met when resolving large strains across the surface rupture (which can exceed 1% strain in most cases, see supplements where we show the differences between the two strain approximations in Figure S2), and is calculated from the following relation using Einstein summation convention,

$$\mathbf{E} = \begin{bmatrix} E_{xx} & E_{xy} \\ E_{yx} & E_{yy} \end{bmatrix}$$

$$E_{\boldsymbol{ij}} = \frac{1}{2}\left(\frac{\Delta u_i}{\Delta x_j} + \frac{\Delta u_j}{\Delta x_i} + \frac{\Delta u_k}{\Delta x_i}\frac{\Delta u_k}{\Delta x_j}\right) \quad (7)$$

To measure contraction and extension along the rupture we calculate the dilatation (i.e., areal strain) from the product of the principal stretches ($1+E_i$, $i = 1, 2$), where positive values denote extension and negative values contraction (Ramsay, 1967). To illustrate areas with different senses of shear and to measure the infinitesimal rotations of regions away from the faulting regions we calculate the vorticity (ω) of the vector field, which is also defined as half the curl (c).

$$\omega = \frac{c}{2} = \frac{1}{2}\left(\frac{\Delta u_x}{\Delta y} - \frac{\Delta u_y}{\Delta x}\right) \quad (8)$$

We note that the vorticity is used primarily to measure the amount of instantaneous local vertical axis rotation of blocks away from faults (which has units of radians) or to illustrate the rotational component of surface motion associated with simple shear strain but it does not measure the shear strain component of simple shear (where ω is defined as half the difference of the off-diagonal components of the displacement gradient tensor [i.e., eq. 8] while the shear strain is the summation). To help illustrate the variation of the total magnitude of strain along the surface rupture we estimate the second invariant of the strain tensor (I_2), which we call the total strain intensity and can be computed from the determinant of $\mathbf{E}$ or,

$$I_2 = \frac{1}{2}\left([\mathrm{tr}(\mathbf{E})]^2 - \mathrm{tr}[\mathbf{E}^2]\right) \quad (9)$$

The fault-zone width is measured from each profile as the average width where the square root of I_2 exceeds a threshold value of 2×10^{-3} which corresponds to 0.2% of the shear strain intensity, and is an amount that corresponds to faulting observed in the field (Ponti et al., 2019; DuRoss et al., 2020).

3 Results

3.1 Distribution of Inelastic Strain

The left-lateral slip distribution of the foreshock rupture shows a simple asymmetric triangular shape, while the mainshock is right-lateral and has a heterogeneous multi-peaked distribution suggesting (Figure 2b). These along-strike variations of slip at different length scales (from 1-10 km) are robust as indicated by the uncertainty in our measurements and may reflect variations due to the fault geometrical roughness and strength or applied stress (Dunham et al., 2011; Shi and Day, 2013; Milliner et al., 2016; Allam et al., 2019; Bruhart et al., 2020), and are an important source of information for scaling relations in probabilistic fault displacement hazard models (Lavrentiadis & Abrahamson, 2019). In addition, the second invariant strain maps clearly show changes of the total strain intensity, which correspond to variations of the fault geometry and orientation along the rupture. The total strain intensity is generally largest at the center of fault segments and systematically dissipates towards their tips in areas of fault bends, branches or en-echelon steps. Along the foreshock rupture we find the mean and maximum left-lateral fault displacements of 0.60 ± 0.03 m (all uncertainties represent 1 standard deviation error, 1σ) and 1.40 ± 0.07 m (1σ), respectively, and for the mainshock rupture the mean and maximum right-lateral displacements of 1.69 ± 0.06 m (1σ) and 4.78 ± 0.22 m (1σ), respectively (Table 1).

To estimate the magnitude of OFD along both ruptures we calculate it as a percent of the total displacement by subtracting the field observations (D_f) (Ponti et al., 2019; DuRoss et al., 2020), which are assumed to capture the primary on-fault displacement, from the total displacement estimated by our optical stacked profiles (which captures both the on- and off-fault deformation across the entire fault zone [D_o]) which is then normalized by D_o, i.e., OFD = $[(D_o - D_f)/D_o] \times 100$. By normalizing the difference of the total and on-fault displacements (measured in meters) by D_o, this allows for more direct comparisons of the amount of off-fault strain between the two ruptures which have different moment magnitudes and amounts of total slip. From this comparison we find OFD is largest near both terminations of the mainshock rupture (see Figure 2 for comparison and Figures S3 and S4) and is overall much larger for the foreshock (mean and median values of 56, 65 ± 15%, 1σ) than the mainshock (mean and median values of 34, 25 ± 15%, 1σ), which have negatively and positively skewed distributions, respectively (Figure S5). Measurements of the fault-zone width show similar widths of inelastic strain between the foreshock and mainshock rupture strands, with mean fault-zone widths of 59 ± 17 m (1σ) and 69 ± 23 m (1σ), respectively (Figure S6).

The 2D dilatational strain maps show it is largest at changes in the geometry of the rupture, where for example, extensional strain (positive dilatation) is largest at sites of right transtensional fault bends (e.g., Figure 3). Along curvilinear segments, where there are subtle changes in the fault orientation, the dilatation varies in sign from negative (contraction) to positive (extensional) over short ~100 m distances that correspond to subtle releasing and restraining bends of the fault (bottom right of Figure 3b along segment i). To understand how the width of the fault-zone may vary according to the type of strain the fault experiences, we compare the fault-zone width measurements along the mainshock rupture from within the transtensional bend (segment ii in Figure 3a) to the linear segment adjacent to it that experienced predominantly shear (segment i). From a comparison of the distributions of the fault-zone widths measured between these two neighboring segments, we find a clear statistical difference (Figure S6). A one-tailed t-test shows that we can reject at the 5% confidence level that the two distributions have the same mean between these two fault segments, indicating there are significantly wider fault zones within the transtensional bend undergoing tension than along the linear segment that experienced mostly shear strain.

To then asses the possible dependency of the fault-zone width with the magnitude of contraction and extension the fault zone experiences we regress the fault-zone widths measured from two km-scale right bends, a linear segment between these bends (Figure 3a) and two short transpressional bends with the magnitude of dilation measured from the 2D dilation strain map. Here we find wider fault zones along the transpressional and transtensional segments and narrowing in regions of decreasing dilatational strain (Figure 4a). To describe this dependency, we use a segment regression analysis, which is a model choice supported by an F-test that shows a piecewise linear function provides a better fit over a linear one even when considering the effect of additional model parameters. Unfortunately, as there are simply not enough transpressional segments or bends along the rupture we are unable to better populate the negative dilatation quadrant in our regression analysis (left side of Figure 4a). In addition, as illustrated by the wide 95% confidence interval bands we do not have sufficient constraint to test with confidence whether fault zones are wider under extension than contraction. Another limitation of the analysis is that due to the sparsity of field measurements along the transtensional segment (segment ii in fig. 3c) there are an insufficient number of OFD points (shown in Figures S3 and S4) to assess how the magnitude of distributed inelastic shear strain may scale with the degree of fault-zone dilatation.

We also find a difference of the spatial distribution of deformation across the fault zone between types of different fault geometries. This can be seen when comparing strain profiles across the transtensional bend (segment ii, Figure 3b) to the adjacent more linear rupture segment to the south (segment i). These profiles show a clear difference in how the inelastic dilatational and shear components of strain decay with distance away from the primary rupture between these two segments (Figure 4c). This suggests that not only can the differences in width of fault-zones be resolved (a scalar quantity) but also the spatial distribution of inelastic strain across segments of different geometries.

The effect of the foreshock rupture with the distribution of strain across and along the mainshock rupture can also be clearly observed at the site where they intersect using the displacement, vorticity and dilatational strain maps (Figure 5). The dilatational strain field shows that the mainshock rupture experienced extension on the segment northwest of the intersection and contraction southeast of the intersection (Figure 5d), which is consistent with the expected location of unclamping and clamping, respectively, due to static stress changes imposed by slip along the foreshock rupture (e.g., Barnhart et al., 2019; Wang et al., 2020; Chen et al., 2020). In addition, we find a noticeable increase of the vorticity along the mainshock rupture that experienced positive dilatation (unclamping) and a decrease along the segment that experienced negative dilatation (clamping) (which are labelled i) and ii) in Figure 5c). These differences in the amount of rotation between the two segments suggests a possible increase in the intensity of simple shear strain but this is not definitive evidence as the vorticity only captures the rotational component of simple shear. Therefore, to verify this we found from displacement profiles that there is indeed a 20 cm increase of the total fault-parallel displacement from the segment that was clamped compared to that which was unclamped (Figure 5f). Profiles that measure the fault-perpendicular motion

(Figure 5g) also clearly show the two fault mainshock rupture segments either side of the intersection experienced clamping (with a total of 50 cm of differential surface motion converging across the fault) and unclamping (a total of 40 cm of differential surface motion diverging away from the fault).

3.2 Bookshelf kinematics

Near the northern termination of the mainshock rupture the vorticity map shows a series of faults that are orthogonal to the main trend of the mainshock rupture that produce a symmetrical 'hourglass' shape (Figure 6). The vorticity maps reveal a series of parallel, NE-trending sinistral shear zones (red regions), that are bracketed to the southeast and northwest by conjugate and almost orthogonally orientated NW-trending dextral faults (blue regions). Between the series of parallel sinistral faults are zones of relatively large vorticity (blue regions in Figure 6a, also see 7a, b). We note that the vorticity cannot differentiate between rotations and distributed fracturing, but due to the pervasive distribution of these high vorticity values and the lack of observed distributed fracturing from field surveying (depicted as black lines in Figures 6a and 7a), the regions between the main faults are likely indicative of rotations of up to ~0.12º. These types of kinematics are indicative of bookshelf faulting, where the conjugate faults and intra-fault block rotations act to collectively accommodate regional dextral shear (McKenzie and Jackson, 1983; Wesnousky, 2005). The different mechanisms by which the regional dextral shear is released can be seen first in the center of Figure 6a, where the total right-lateral shear is accommodated by a single dextral fault strand with a total offset ~1.6 m, this offset is then partitioned further south between three parallel dextral fault strands, and then partitioned again further south amongst the conjugate sinistral faults and clockwise rotating blocks (Figure 6a and 7a, b).

To quantify whether the observed kinematics are actually consistent with bookshelf faulting, we compare the surface motions measured in our displacement and vorticity maps to the kinematic relations of a bookshelf fault system (McKenzie and Jackson, 1983; Platt and Becker, 2013). If the regional right-lateral shear displacement (γ) and the angle between the conjugate and bounding faults (α) are known, then the amount of sinistral slip along the array of conjugate faults (γ')

expected from bookshelf faulting can be estimated from the following geometric relation (also see inset of Figure 6c).

$$\gamma' = \gamma \cdot \cos(2\alpha) \tag{10}$$

The rotation of the blocks (ω) can be estimated from eq. 11 and assuming horizontal plane strain, a component of contractional or extensional strain normal to the fault blocks (e) can be estimated from eq. 12, where l_b is the block length.

$$\omega = \frac{\gamma}{2} \cdot (1 - \cos[2\alpha]) \tag{11}$$

$$e = -\frac{\gamma}{2l_b} \cdot \sin(2\alpha) \tag{12}$$

From these relations and measuring $\gamma = 1.6$ m and $\alpha = 66°$ (from Figure 6a) this predicts $\gamma' = 1.0$ m, e=0.044% strain and $\omega = 0.05°$ (see Table 2). These predicted values compare well with those observed from the strain and displacement maps (Figure 6a and 7), where we find $\gamma' = 0.8$ m (measured from the southernmost sinistral fault), e=0.04% strain (measured from within the bookshelf blocks, see Figure S7) and $\omega = 0.06°$ (mean value estimated from within the southernmost 'block' in Figure 6), which show the observed kinematics are consistent with bookshelf faulting.

To test whether the foreshock and mainshock cross-faulting are a larger-scale version of the same bookshelf tectonics shown in Figure 6a and c, we again use the kinematic bookshelf relations to compare its predictions against the observed displacements at the macroscopic scale (McKenzie and Jackson, 1983; Platt and Becker, 2013). From measuring the mean slip along the mainshock strand immediately adjacent to the foreshock strand we find γ= 0.98 m and the angle between the mainshock-foreshock strands is $\alpha = 86°$. From this we find the predicted slip on the foreshock fault is $\gamma' = 0.97$ m which falls within the variation of observed values (mean observed sinistral displacement of 0.71 ± 0.33 m, 1σ, and maximum of 1.40 m, Figure 2).

We can also estimate the total amount of long-term cumulative displacement (d_{fore}) accrued along the conjugate sinistral foreshock fault (the strand west of the mainshock strand) since its initiation. To do this we use a simple geometric expression that relates d_{fore} to the amount of total block rotation that has occurred across a zone of simple shear (Freund, 1974; Ron et al., 1984). Assuming only plane strain, d_{fore} is related to: the width of fault-bounded blocks (w_b, see Figure 6c), the initial angle between the conjugate faults when they first formed (α_i) and the total amount of rotation since they formed (ω_T) as defined by the following relation (Freund, 1974; Ron et al., 1984),

$$d_{fore} = w_b \left[\frac{\sin(\omega_T)}{\sin(\alpha)\cdot\sin(\alpha-\omega_T)}\right] \tag{13}$$

The width of the block (w_b = 4.89 km) is measured as the distance between the foreshock fault west of the mainshock strand to another parallel SW-trending fault to the south (see Figure 6c). This gives an aspect ratio of the crustal block (width/length) of 0.37 which is consistent with the aspect ratios of the smaller blocks in Figure 6a, that have a mean value of 0.35 (n = 5). The total amount of rotation of the foreshock fault (ω_T= 3-7°) is estimated from the difference of its average azimuth (N43°E) with the azimuth of the smaller conjugate sinistral faults shown in Figure 6a (with minimum and maximum values ranging from N36-40°E). This assumes that the much shorter sinistral faults (ranging in lengths from 200 – 1300 m) shown in Figure 6a are close to their initial orientation when they developed. The initial angle between the conjugate foreshock faults and the bounding dextral mainshock faults is assumed as α = 90° (a value also used for conjugate faults further north in the Walker Lane [see Wesnousky, 2005]). This gives d_{fore} = 256-600 m, which indicates that the foreshock fault is highly structurally immature.

4. Discussion

4.1. Effect of Off-fault Deformation on Rupture

Experimental and theoretical studies show that the rupture propagation through the near-surface (< 5 km depth) can be inhibited by a range of mechanisms, including velocity-strengthening frictional properties of the sliding fault in the near-surface, generation of plastic strain during rupture, and frictional sliding on pre-existing fractures that can dissipate the rupture energy (Fialko et al., 2005; Sammis et al., 2010; Kaneko and Fialko, 2011; Gabriel et al., 2013). These mechanisms may explain why some earthquakes exhibit significantly lower slip at the surface than at seismogenic depths (6-10 km), which has been termed the shallow slip deficit (Fialko et al., 2005), and why ruptures with faster velocities are observed along more mature structurally developed smoother faults, e.g., the 1999 M_w 7.4 Izmit, 2001 M_w 7.8 Kokoxili, 2002 M_w 7.9 Denali and 2018 M_w 7.5 Palu earthquakes (Bouchon et al., 2001, 2010; Ozacar and Beck, 2004; Bao et al., 2019; Socquet et al., 2019).

As faults accumulate displacement over geologic timescales, they are thought to evolve or 'mature' progressively from a network of disorganized and disconnected segments that are separated by geometrical complexities (such as stepovers, bends and branches), to a structurally simplified system or sometimes single throughgoing fault (Tchalenko, 1970; Wesnousky, 1988; Stirling et al., 1996). This structural evolution can occur via a range of fault growth and strain weakening feedback processes (Ben-Zion & Sammis, 2003; Faulkner & Mitchell, 2011). A consequence of this evolutionary process is that as strain progressively localizes to the fault core, distributed fractures become abandoned (Frost et al., 2009). This is manifest by a decreasing density of stepovers at the macroscopic scale (Wesnousky, 1988) and decreasing amounts of distributed off-fault inelastic strain (Dolan and Haravitch, 2014; Frost et al., 2009). Here we find OFD for the foreshock is much larger than the mainshock (56% and 34% respectively), which we interpret as indicating the faults involved in the foreshock rupture have a lower degree of strain localization and are therefore less structurally developed (Dolan and Haravitch, 2014). To support this inference, we have assessed a number of other relevant factors, which includes both qualitatively and quantitively comparing the geometrical fault complexity of the foreshock to the mainshock. First, surface rupture mapping from daily Planet Labs imagery, which can uniquely separate the two events in time (Milliner & Donnellan, 2020), show the foreshock is clearly more structurally complex with a higher number of disorganized segments (see Figure S8). Second, from estimating the density of major stepovers (> 1 km width, following the approach of Wesnousky [1988]) we find it is almost a factor of two higher for the foreshock (0.157 stepovers/unit length) than the mainshock (0.08), again showing the foreshock involved a more disconnected fault system. Lastly, measurements of offset Jurassic felsic dikes across the southern end of the Ridgecrest mainshock rupture found a cumulative displacement of 1.6 km, although there are no available geomorphic features to estimate a value across the foreshock rupture (Andrew & Walker, 2020). However, this value of 1.6 km is much larger than our estimated cumulative displacement for the foreshock rupture of 256-600 m, suggesting a clear difference in the structural maturity. Although there is not a known independent estimate of the cumulative displacement for the foreshock rupture to verify possible differences in the relative structural maturity of the faults involved in the two ruptures, our results do show clear differences in the degree of strain localization, structural organization and significant differences in estimates of the cumulative displacement assuming bookshelf type kinematics.

Here, we assess whether faults that have larger OFD (i.e., larger amounts of distributed inelastic strain and are therefore likely less mature), have slower rupture velocities and more pronounced shallow slip deficits. Estimates of the mean OFD along the mainshock rupture (34 ± 10%) is similar to that measured along nearby surface ruptures using a similar approach used here (from comparison of the optical and field-based displacements), which are fault systems that are known to be immature, which include the 1992 Landers and 1999 Hector Mine ruptures (with OFD of 46 ± 10% and 39 ± 22%, respectively [Milliner et al., 2016]). Interestingly, all three of these relatively immature NW-trending dextral fault systems exhibit relatively similar slow rupture velocities of ~2.7 km/, 2.2 km/s, and 2 km/s for the Landers, Hector Mine and Ridgecrest events, respectively (Chen et al., 2020; Goldberg et al., 2020; Ji et al., 2002; Liu et al., 2019; Peyrat et al., 2001; Ross et al., 2019), consistent with the notion that slower ruptures occur along faults of higher OFD with more complex multi-segment rupture geometries.

The larger amount of OFD found for the foreshock (56%) than the mainshock rupture (34%), provides another and more direct means to compare the possible effect of off-fault distributed strain on the shallow slip deficit and rupture velocity. Current seismic inversion models of the rupture do not show a significant difference of the velocity between the two events, finding they are both ~2 km/s (Chen et al., 2020; Goldberg et al., 2020; Ross et al., 2019; Wang et al., 2020). However, the lack of a resolvable difference could result from limitations of the inversion method such as the model resolution, data constraints and sensitivity, or inherent trade-offs (e.g., see Figure S4 of Chen et al., 2020 for the range of possible velocities). An additional complication is that it is possible the mainshock rupture velocity could have been inhibited by a decrease of static

Coulomb stress applied by the foreshock rupture, as high shear pre-stresses along faults are thought to cause faster rupture velocities (Bao et al., 2019). However, the effect of reduced shear pre-stress is likely to be small in this case, given inverted slip models estimate a minor amount (~-0.2 MPa) compared to the total stress drop (10 MPa), (Barnhart et al., 2019; Chen et al., 2020). Therefore, it is not clear if the rupture velocities between the foreshock and mainshock are significantly similar or not, or could result from pre-stress changes that inhibited rupture propagation.

To assess differences in the variation of slip with depth between the M_w 6.4 foreshock and M_w 7.1 mainshock events we compiled slip distributions from the available geodetic and seismic slip inversion studies (Chen et al., 2020; Jin and Fialko, 2019; Xu et al., 2020; Wang et al., 2020). Although there is a wide variation of the slip-depth distributions between the various slip inversion models, which reflects the epistemic uncertainty due to varying model parameterizations, inversion strategies and data types, there are still systematic differences between the foreshock and mainshock events (Figure 7). Estimating the shallow slip deficit as the percent difference of surface slip to the maximum at depth, we find a more pronounced shallow slip deficit for the foreshock (ranging from 42-65%) than the mainshock (18-35%), consistent with the notion that more immature faults that exhibit larger amounts of inelastic strain (i.e., OFD) correspond to larger shallow slip deficits (as proposed by Kaneko & Fialko, 2011). In contrast, shallow slip deficit estimates of the 1992 Landers and 1999 Hector Mine events from geodetic inversions show much smaller values at 18% and 3%, respectively (Xu et al., 2016). The apparent similar amounts of inelastic strain (34%, 46% and 39% OFD) but differing shallow slip deficits (18-35%, 18%, and 3%) between these three large events (Ridgecrest, Landers and Hector Mine, respectively) conflicts with the expectation that the former may influence the latter. This may suggest the importance of other processes in affecting the efficiency of rupture propagation through the near-surface such as sediment thickness and type, pre-stress on the fault, frictional properties, or dilatancy strengthening (Rice, 1975; Marone et al., 1991; Kaneko and Fialko, 2011; Dolan and Haravitch, 2014).

4.2. Inelastic strain and the effect of fault-zone dilatation

From comparison of the measured fault-zone width with the dilatational component of the 2D strain tensor we find that both the scalar width and rate of dissipation of inelastic strain away from the main rupture are wider and slower in regions of extension and contraction than shear (Figure 4). The magnitude and sense of dilatational strain (i.e., contraction or extension), varies according to the fault geometry and orientation, with extensional strain expectedly largest along releasing fault bends (Figures 3 and 4). This is consistent with previous work that have found correlations of the scalar fault width or OFD with the fault geometry along oblique-normal strike-slip faults (Scott et al., 2018; Teran et al., 2015). Along the Ridgecrest rupture we have shown that these geometries alter the type of strain the fault-zone experiences and that strain is partitioned differently between the shear and dilatational components (Figure 4b and c).

Constraining how fast or slow inelastic strain decays away from the primary rupture holds importance for better characterizing the hazard of distributed fault rupture, which is needed to effectively engineer structures to withstand its effect (e.g., for roads, pipelines or bridges that cannot avoid fault crossings). As more confidence is known of what parameters control the spatial distribution of inelastic strain across a surface rupture (e.g., the type of fault geometry or sediment thickness) through increasing observational constraint, this will help explain more of the total variation of the fault-zone width along the lengths of ruptures. In doing so this will reduce the epistemic uncertainty of empirically constrained probabilistic fault displacement hazard models and improve their predictive power (e.g., Petersen et al., 2011). For example, our results show that transtensional bends have a different level of distributed rupture hazard, with a higher probability of experiencing distributed rupture further away from the primary fault, than segments that experience predominantly shear strain (Figure 4b and c). This would therefore justify developing separate fault displacement prediction equations for differing fault geometries into probabilistic fault displacement hazard analysis.

4.3 Orthogonal faulting due to Bookshelf kinematics

Bookshelf faulting is thought to initiate from simple shear being accommodated by conjugate pairs of synthetic (R) and antithetic (R’) Riedel shears across a trans-tensional step-over region (Wesnousky, 2005). Over time, as the Riedel fractures accumulate slip, the primary *en-echelon* R shears coalesce to form a single through-going fault strand, while the R' shears located within the stepover are progressively rotated and become increasingly more oblique to the R shears, eventually forming a set of orthogonal faults. Here, we find that the observed displacements along the orthogonal set of faults involved in the foreshock and mainshock ruptures are consistent with predictions of bookshelf kinematics indicating they are a larger scale, more-developed system of the bookshelf faulting observed at the smaller scale in Fig 6a and c. In addition, the asymmetric triangular distribution of slip along the foreshock rupture (at the ~10 km scale) bears a strong similarity to that of slip along the smaller sinistral conjugate faults shown in Figure 6a (at the ~100 m scale, also see Figure S9 for comparison). Such bookshelf faulting which involves progressive rotation of conjugate faults to orientations that become highly mis-aligned could also explain the wide-spread distribution of orthogonal aftershocks at other length scales in this region (Ross et al., 2019). A bookshelf system at the ~10 km scale also suggests that the Little Lake Fault Zone (LLFZ) would be the west-most bounding NW-trending dextral fault. This provides a possible explanation as to why the foreshock rupture terminated surprisingly at a site of peak slip in the southwest (~1.4 m, Figure 2), simply because it is structurally controlled by the bookshelf kinematics; i.e., west of the LLFZ there are likely no rotations of crustal blocks and therefore sinistral slip is not kinematically required and thus the foreshock fault simply does not extend further west.

However, one notable difference from the bookshelf initiation framework proposed by Wesnousky (2005) is that the bookshelf faulting found specifically at the northern end of the mainshock rupture (Figures 6 and 7) does not seem to occur within a transtensional step. Here there are clearly no dextral faults that extend to either side to 'bound' the sinistral faults that would satisfy the definition of a stepover, nor does the rupture step to the left that would produce transtension and the dilatation map shows no evidence of significant extension. Instead, the clockwise rotation and sinistral faulting found here are located directly beyond the tips of and between three north-west trending dextral faults (one to the north and the other two to the south), producing an 'hourglass' geometry. We argue another possible mechanism in which bookshelf kinematics could arise is due to the transition of shear strain to rotation beyond fault tips (like that shown by the vorticity map, Figure 6a). In the case here, two or more faults do not align or connect, which creates a zone of distributed clockwise rotation. For the dextral shear to be accommodated over a region (in this case this is ~2 m of dextral motion distributed over an ~1.5 km wide zone across the ‘bookshelf’, see Figure 7d) it can be shown that it requires both clockwise rotation (illustrated in Figure 6a and 7d) and perpendicular sinistral shear (shown in Figure 7c, where such strain is responsible for producing the series of parallel sinistral fractures), as the summation of the displacement gradients of both these types of surface motion are equivalent to dextral shear and does not require transtensional strain (Platt, 2017). A similar behavior of bookshelf faulting was also observed from relocated aftershocks of the 1986 M_L 5.7 Mount Lewis earthquake, CA (Kilb et al. 2002). The seismicity showed a series of orthogonal sinistral faults that were not located within a stepover but instead directly beyond the tips of a dextral fault, which produced a similar ‘hourglass’ shaped feature as observed here. For the kinematics found specifically at the northern end of the Ridgecrest rupture, the cause of bookshelf faulting seems to be more consistent with how shear strain transitions beyond fault tips to rotation (i.e., a type of fault termination structure) than a result of distributed transtensional shear across a right-stepover which is a mechanism more applicable to faulting within the Mina deflection further north in the Walker Lane (Wesnousky, 2005).

A number of major northwest trending dextral faults in the ECSZ seem to stop abruptly at major orthogonally orientated sinistral faults (such as the Garlock or Pinto Mountain faults, see Figure 6e). The lack of a physical connection makes it unclear how the regional right-lateral shear strain is accommodated across these fault gaps and how these junctions evolve over geologic timescales. A lack of paleomagnetic data specifically at these fault gaps also make it difficult to understand the role of crustal rotations in accommodating this long-term regional dextral strain. Here the vorticity map shows clear regions of relatively large clockwise rotation adjacent to NE-trending sinistral faults (Figure 6a). Observations from field mapping of the rupture do not show pervasive fracturing in these regions, which confirms that much of the large positive vorticity values most likely reflect crustal rotations (that range up to ~0.1º). The vorticity map also shows that neither the northern nor the southern set of conjugate sinistral faults (i.e., within either end of the ‘hourglass’ feature) intersect or displace the NW-trending dextral faults but are instead embedded within regions of clockwise rotation. This provides one possible explanation as to why NW-trending dextral faults do not physically connect with neighboring NE-trending sinistral faults, simply because dextral brittle shear strain transitions beyond their tips to zones of clockwise rotation as previously hypothesized (Andrew and Walker, 2017). As mentioned previously, dextral shear is kinematically equivalent to the sum of surface motion from orthogonally orientated sinistral shear and clockwise rotation (Platt, 2017). Therefore our observations of coseismic strain release we believe are analogous and support the kinematic argument that the remaining component of long-term dextral strain across regions of fault gaps is likely accommodated by clockwise rotation explaining the lack of physical connection (i.e., that shown in Figure 6a).

Conclusions

Measurements of surface motion across the Ridgecrest surface rupture from high-resolution optical image correlation provide empirical constraints of the effect of contraction and extension on the width of the fault-zone. The results show that as expected, faults are clearly wider under extension and contraction than lateral shear, but we are unable to discern whether they are wider under extension than contraction. This relation also helps explain the apparent correlation of fault geometrical complexities with wider faults zones, as variations of the fault orientation alter the local stress state, causing fault-perpendicular strain that is not equally partitioned across the fault-zone between the dilatational and shear strain components. Observations of how the inelastic strain attenuates with distance from the primary rupture (Figure. 4 b, c) also suggests there are different hazard probabilities of distributed rupture for transpressional and transtensional bends compared to simpler, more linear segments of the rupture that experience predominantly shear strain. We suggest these differences could be accounted for by developing separate fault displacement prediction equations for different fault geometries when incorporating them into probabilistic fault displacement hazard analysis (PFDHA).

Our analysis shows that the faults involved in both the foreshock and mainshock ruptures are both structurally immature and that the former is likely less structurally developed as we find a higher amount of distributed inelastic strain for the former (with average off-fault deformation amounts of 56 ± 10% and 34 ± 10 %, respectively). The structural immaturity of the foreshock faults is also supported by an estimate of its cumulative displacement, which is found from approximating the kinematics to bookshelf motion, that gives a relatively low total amount of 250-600 m. The larger amount of off-fault deformation and inferred lower structural maturity for the foreshock faults shows a fault system with higher amounts of near-surface distributed inelastic strain and poorer fault linkage. These are all thought to affect the efficiency of rupture propagation through the shallow surface, which could explain why the foreshock rupture exhibits a higher slip deficit than the more mature and structurally simplified mainshock rupture (Wesnousky, 1988; Kaneko & Fialko, 2011; Dolan and Haravitch, 2014).

We propose that bookshelf faulting provides a concise and useful framework to explain a number of questions regarding the faulting kinematics of this region at the local and regional scale. Our measurements of 2D strain and rotation show, i) faults do not intersect one another because dextral strain transitions to clockwise rotation beyond their tips, ii) cross-faulting and aftershock distributions arise because of progressive clockwise rotation of conjugate faults that accommodate simple shear, iii) the foreshock-mainshock ruptures are likely a larger scale version of 'bookshelf faulting' which can explain the southwestern termination point of the foreshock event because it structurally abuts the Little Lake fault zone that marks the west-bounding 'bookshelf' fault.

Acknowledgements

We would like to thank the reviewers, Chelsea Scott and Mike Oskin for their helpful suggestions and Isabelle Manighetti for comments that helped strengthen and clarify aspects of our study. We also thank Alex Morelan, Tim Dawson, Kate Scharer, for their helpful discussions and sharing of data as well as many others who cannot all be mentioned here for helping provide detailed field survey measurements of the surface ruptures. **Funding**: Part of this research was supported by the NASA Earth Surface and Interior focus area and performed at the Jet Propulsion Laboratory, California Institute of Technology (80NM0018D0004). Funding for this project was provided under a NASA Postdoctoral Program fellowship to C.M. administered by the Universities Space and Research Association through a contract with NASA. Satellite imagery for this project were purchased under SCEC grant #19222. **Author contributions**: All authors contributed to this study and participated in manuscript revision. Competing interests: The authors declare that they have no competing interests. **Data and materials availability**: Please see supplementary datasets or the Zenodo open repository (http://doi.org/10.5281/zenodo.3937853) containing measurements of the coseismic fault slip, fault-zone width and off-fault deformation

References

Allam A.A., Kroll K.A., Milliner C.W., Richards-Dinger K.B. Effects of fault roughness on coseismic slip and earthquake locations. Journal of Geophysical Research: Solid Earth. 2019 Nov;124(11):11336-49

Amos, C.B., Brownlee, S.J., Rood, D.H., Fisher, G.B., Bürgmann, R., Renne, P.R. and Jayko, A.S., 2013. Chronology of tectonic, geomorphic, and volcanic interactions and the tempo of fault slip near Little Lake, California. *Bulletin*, *125*(7-8), pp.1187-1202.

Anderson, E.M., 1951. The dynamics of faulting and dyke formation with applications to Britain. Oliver and Boyd, Edinburgh.

Andrew, J.E., Walker, J.D. and Monastero, F.C., 2015. Evolution of the central Garlock fault zone, California: A major sinistral fault embedded in a dextral plate margin. *Bulletin*, *127*(1-2), pp.227-249.

Andrew, J.E., Walker, J.D., 2017. Path and amount of dextral fault slip in the Eastern California shear zone across the central Mojave Desert. GSA Bull. 129, 855–868. https://doi.org/10.1130/B31527.1

Andrew J.E., Walker, J.D., 2020, Total Slip Estimates of the M7.1 (July 2019) Seismogenic Airport Lake Fault System, Ridgecrest, California, GSA meeting. Abstract: 31-4

Bao, H., Ampuero, J.-P., Meng, L., Fielding, E.J., Liang, C., Milliner, C.W.D., Feng, T., Huang, H., 2019. Early and persistent supershear rupture of the 2018 magnitude 7.5 Palu earthquake. Nat. Geosci. 12, 200–205. https://doi.org/10.1038/s41561-018-0297-z

Barnhart, W.D., Hayes, G.P., Gold, R.D., 2019. The July 2019 Ridgecrest, California, Earthquake Sequence: Kinematics of Slip and Stressing in Cross-Fault Ruptures. Geophys. Res. Lett. 46, 11859–11867. https://doi.org/10.1029/2019GL084741

Becker, T.W., Hardebeck, J.L., Anderson, G., 2005. Constraints on fault slip rates of the southern California plate boundary from GPS velocity and stress inversions. Geophys. J. Int. 160, 634–650. https://doi.org/10.1111/j.1365-246X.2004.02528.x

Ben-Zion Y, Sammis CG. Characterization of fault zones. Pure and applied geophysics. 2003 Mar 1;160(3-4):677-715.

Bouchon, M., Bouin, M.-P., Karabulut, H., Toksöz, M.N., Dietrich, M., Rosakis, A.J., 2001. How fast is rupture during an earthquake? New insights from the 1999 Turkey Earthquakes. Geophys. Res. Lett. 28, 2723–2726. https://doi.org/10.1029/2001GL013112

Bouchon, M., Karabulut, H., Bouin, M.-P., Schmittbuhl, J., Vallée, M., Archuleta, R., Das, S., Renard, F., Marsan, D., 2010. Faulting characteristics of supershear earthquakes. Tectonophysics 493, 244–253. https://doi.org/10.1016/j.tecto.2010.06.011

Brandenberg, S.J., Stewart, J.P., Wang, P., Nweke, C.C., Hudson, K., Goulet, C.A., Meng, X., Davis, C.A., Ahdi, S.K., Hudson, M.B., Donnellan, A., Lyzenga, G., Pierce, M., Wang, J., Winters, M.A., Delisle, M.-P., Lucey, J., Kim, Y., Gallien, T.W., Lyda, A., Yeung, J.S., Issa, O., Buckreis, T., Yi, Z., 2020. Ground Deformation Data from GEER Investigations of Ridgecrest Earthquake Sequence. Seismol. Res. Lett. https://doi.org/10.1785/0220190291

Brooks, B.A., Minson, S.E., Glennie, C.L., Nevitt, J.M., Dawson, T., Rubin, R., Ericksen, T.L., Lockner, D., Hudnut, K., Langenheim, V., Lutz, A., Mareschal, M., Murray, J., Schwartz, D., Zaccone, D., 2017. Buried shallow fault slip from the South Napa earthquake revealed by near-field geodesy. Sci. Adv. 3, e1700525. https://doi.org/10.1126/sciadv.1700525

Bruhat L, Klinger Y, Vallage A, Dunham EM. Influence of fault roughness on surface displacement: from numerical simulations to coseismic slip distributions. Geophysical Journal International. 2020 Mar;220(3):1857-77.

Chen, K., Avouac, J.-P., Aati, S., Milliner, C., Zheng, F., Shi, C., 2020. Cascading and pulse-like ruptures during the 2019 Ridgecrest earthquakes in the Eastern California Shear Zone. Nat. Commun. 11, 22. https://doi.org/10.1038/s41467-019-13750-w

Dawson, T.E., McGill, S.F. and Rockwell, T.K., 2003. Irregular recurrence of paleoearthquakes along the central Garlock fault near El Paso Peaks, California. Journal of Geophysical Research: Solid Earth, 108(B7). doi.org/10.1029/2001JB001744

Dolan, J.F. and Haravitch, B.D., 2014. How well do surface slip measurements track slip at depth in large strike-slip earthquakes? The importance of fault structural maturity in controlling on-fault slip versus off-fault surface deformation. *Earth and Planetary Science Letters*, *388*, pp.38-47.

Dolan, J.F., McAuliffe, L.J., Rhodes, E.J., McGill, S.F., Zinke, R., 2016. Extreme multi-millennial slip rate variations on the Garlock fault, California: Strain super-cycles, potentially time-variable fault strength, and implications for system-level earthquake occurrence. Earth Planet. Sci. Lett. 446, 123–136. https://doi.org/10.1016/j.epsl.2016.04.011

Dor O, Ben-Zion Y, Rockwell TK, Brune J. Pulverized rocks in the Mojave section of the San Andreas Fault Zone. (2006) Earth and Planetary Science Letters. May 30;245(3-4):642-54.

DuRoss, C. B., R. D. Gold, T. E. Dawson, K. M. Scharer, K. J. Kendrick, S. O. Akciz, S. J. Angster, J. Bachhuber, S. Bacon, S. EK. Bennett, et al. (2020). Surface Displacement Distributions for the July 2019 Ridgecrest, California, Earthquake Ruptures, Bull. Seismol. Soc. Am. XX, 1–19, doi: 10.1785/0120200058

Dunham, E.M., Belanger, D., Cong, L., Kozdon, J.E., 2011. Earthquake Ruptures with Strongly Rate-Weakening Friction and Off-Fault Plasticity, Part 1: Planar FaultsEarthquake Ruptures with Strongly Rate-Weakening Friction and Off-Fault Plasticity, Part 1: Planar Faults. Bull. Seismol. Soc. Am. 101, 2296–2307. https://doi.org/10.1785/0120100075

Dziewonski, A. M., T.-A. Chou and J. H. Woodhouse, 1981, Determination of earthquake source parameters from waveform data for studies of global and regional seismicity, J. Geophys. Res., 86, 2825-2852, 1981. doi:10.1029/JB086iB04p02825

Ekström, G., M. Nettles, and A. M. Dziewonski, 2012, The global CMT project 2004-2010: Centroid-moment tensors for 13,017 earthquakes, Phys. Earth Planet. Inter., 200-201, 1-9,. doi:10.1016/j.pepi.2012.04.002

Faulkner DR, Mitchell TM, Jensen E, Cembrano J. Scaling of fault damage zones with displacement and the implications for fault growth processes. Journal of Geophysical Research: Solid Earth. 2011 May;116(B5).

Fialko, Y., Sandwell, D., Simons, M., Rosen, P., 2005. Three-dimensional deformation caused by the Bam, Iran, earthquake and the origin of shallow slip deficit. Nature 435, 295. https://doi.org/10.1038/nature03425

Frankel, K.L., Glazner, A.F., Kirby, E., Monastero, F.C., Strane, M.D., Oskin, M.E., Unruh, J.R., Walker, J.D., Anandakrishnan, S., Bartley, J.M., Coleman, D.S., Dolan, J.F., Finkel, R.C., Greene, D., Kylander-Clark, A., Marrero, S., Owen, L.A., Phillips, F., 2008. Active tectonics of the eastern California shear zone, in: GSA Field Guide 11: Field Guide to Plutons, Volcanoes, Faults, Reefs, Dinosaurs, and Possible Glaciation in Selected Areas of Arizona, California, and Nevada. Geological Society of America, pp. 43–81. https://doi.org/10.1130/2008.fld011(03)

Freund, R., 1974. Kinematics of transform and transcurrent faults. Tectonophysics 21, 93–134. https://doi.org/10.1016/0040-1951(74)90064-X

Frost E, Dolan J, Sammis C, Hacker B, Cole J, Ratschbacher L. (2009) Progressive strain localization in a major strike-slip fault exhumed from midseismogenic depths: Structural observations from the Salzach-Ennstal-Mariazell-Puchberg fault system, Austria. Journal of Geophysical Research: Solid Earth. Apr;114(B4).

Gabriel, A.-A., Ampuero, J.-P., Dalguer, L.A., Mai, P.M., 2013. Source properties of dynamic rupture pulses with off-fault plasticity. J. Geophys. Res. Solid Earth 118, 4117–4126. https://doi.org/10.1002/jgrb.50213

Ganev, P.N., Dolan, J.F., McGill, S.F., Frankel, K.L., 2012. Constancy of geologic slip rate along the central Garlock fault: implications for strain accumulation and release in southern California. Geophys. J. Int. 190, 745–760. https://doi.org/10.1111/j.1365-246X.2012.05494.x

Gold, R.D., Reitman, N.G., Briggs, R.W., Barnhart, W.D., Hayes, G.P., Wilson, E., 2015. On- and off-fault deformation associated with the September 2013 Mw 7.7 Balochistan earthquake: Implications for geologic slip rate measurements. Tectonophysics 660, 65–78. https://doi.org/10.1016/j.tecto.2015.08.019

Goldberg, D.E., Melgar, D., Sahakian, V.J., Thomas, A.M., Xu, X., Crowell, B.W., Geng, J., 2020. Complex Rupture of an Immature Fault Zone: A Simultaneous Kinematic Model of the 2019 Ridgecrest, CA Earthquakes. Geophys. Res. Lett. 47, e2019GL086382. https://doi.org/10.1029/2019GL086382

Hardebeck, J. L. (2020). A Stress-Similarity Triggering Model for Aftershocks of the Mw 6.4 and 7.1 Ridgecrest Earthquakes, Bull. Seismol. Soc. Am. 110, 1716–1727, doi: 10.1785/0120200015

Hatem AE, Cooke ML, Toeneboehn K. Strain localization and evolving kinematic efficiency of initiating strike-slip faults within wet kaolin experiments. Journal of Structural Geology. 2017 Aug 1;101:96-108.

Hauksson E. State of stress from focal mechanisms before and after the 1992 Landers earthquake sequence. Bulletin of the Seismological Society of America. 1994 Jun 1;84(3):917-34.

Herbert, J.W., Cooke, M.L., Oskin, M., Difo, O., 2014. How much can off-fault deformation contribute to the slip rate discrepancy within the eastern California shear zone? Geology 42, 71–75. https://doi.org/10.1130/G34738.1

Hudnut, K.W., Seeber, L., Pacheco, J., 1989. Cross-fault triggering in the November 1987 Superstition Hills Earthquake Sequence, southern California. Geophys. Res. Lett. 16, 199–202. https://doi.org/10.1029/GL016i002p00199

Jachens, R.C., Langenheim, V.E., Matti, J.C., 2002. Relationship of the 1999 Hector Mine and 1992 Landers Fault Ruptures to Offsets on Neogene Faults and Distribution of Late Cenozoic Basins in the Eastern California Shear Zone. Bull. Seismol. Soc. Am. 92, 1592–1605. https://doi.org/10.1785/0120000915

Ji, C., Wald, D.J., Helmberger, D.V., 2002. Source Description of the 1999 Hector Mine, California, Earthquake, Part I: Wavelet Domain Inversion Theory and Resolution Analysis. Bull. Seismol. Soc. Am. 92, 1192–1207. https://doi.org/10.1785/0120000916

Jin, Z., Fialko, Y.A., 2019. Rupture models of the 2019 M6.4-7.1 Ridgecrest earthquakes constrained by space geodetic data and aftershock locations. 1 Fall Meet. Abstr. 31.

Johnson, K.M., 2013. Slip rates and off-fault deformation in Southern California inferred from GPS data and models. *Journal of Geophysical Research: Solid Earth*, *118*(10), pp.5643-5664.

Kaneko, Y., Fialko, Y., 2011. Shallow slip deficit due to large strike-slip earthquakes in dynamic rupture simulations with elasto-plastic off-fault response. Geophys. J. Int. 186, 1389–1403. https://doi.org/10.1111/j.1365-246X.2011.05117.

Kilb, D. and Rubin, A.M., 2002. Relocated microearthquakes of the Mt. Lewis ML5. 7, California, earthquake sequence: Implications of diverse fault orientations. *Journal of Geophysical Research*, *107*, p.2294.

Kreemer, C., Blewitt, G., Klein, E.C., 2014. A geodetic plate motion and Global Strain Rate Model. Geochem. Geophys. Geosystems 15, 3849–3889. https://doi.org/10.1002/2014GC005407

Lavrentiadis G, Abrahamson N. Generation of Surface-Slip Profiles in the Wavenumber Domain. Bulletin of the Seismological Society of America. 2019 Jun;109(3):888-907.

Li, Y. G., and J. E. Vidale (2001), Healing of the shallow fault zone from 1994–1998 after the 1992 M7.5 Landers, California, earthquake, Geophys. Res. Lett., 28, 2999–3002, doi:10.1029/2001GL012922.

Liu, C., Lay, T., Brodsky, E.E., Dascher-Cousineau, K., Xiong, X., 2019. Coseismic Rupture Process of the Large 2019 Ridgecrest Earthquakes From Joint Inversion of Geodetic and Seismological Observations. Geophys. Res. Lett. 46, 11820–11829. https://doi.org/10.1029/2019GL084949

Marone, C.J., Scholtz, C.H., Bilham, R., 1991. On the mechanics of earthquake afterslip. J. Geophys. Res. Solid Earth 96, 8441–8452. https://doi.org/10.1029/91JB00275

McClusky, S.C., Bjornstad, S.C., Hager, B.H., King, R.W., Meade, B.J., Miller, M.M., Monastero, F.C., Souter, B.J., 2001. Present day kinematics of the Eastern California Shear Zone from a geodetically constrained block model. Geophys. Res. Lett. 28, 3369–3372. https://doi.org/10.1029/2001GL013091

McGill, S.F., Wells, S.G., Fortner, S.K., Kuzma, H.A., McGill, J.D., 2009. Slip rate of the western Garlock fault, at Clark Wash, near Lone Tree Canyon, Mojave Desert, CaliforniaSlip rate of the western Garlock fault. GSA Bull. 121, 536–554. https://doi.org/10.1130/B26123.1

McGuire, R.K., 1995. Probabilistic seismic hazard analysis and design earthquakes: Closing the loop. Bull. Seismol. Soc. Am. 85, 1275–1284.

McKenzie, D., Jackson, J., 1983. The relationship between strain rates, crustal thickening, palaeomagnetism, finite strain and fault movements within a deforming zone. Earth Planet. Sci. Lett. 65, 182–202. https://doi.org/10.1016/0012-821X(83)90198-X

Meade, B.J., Hager, B.H., 2005. Block models of crustal motion in southern California constrained by GPS measurements. J. Geophys. Res. Solid Earth 110. https://doi.org/10.1029/2004JB003209

Miller, D.M. and Yount, J.C., 2002. Late Cenozoic tectonic evolution of the north-central Mojave Desert inferred from fault history and physiographic evolution of the Fort Irwin area, California. *Geologic evolution of the Mojave Desert and southwestern basin and range: Geological Society of America Memoir*, *195*, pp.173-198.

Milliner, C.W.D., Dolan, J.F., Hollingsworth, J., Leprince, S., Ayoub, F., 2016. Comparison of coseismic near-field and off-fault surface deformation patterns of the 1992 Mw 7.3 Landers and 1999 Mw 7.1 Hector Mine earthquakes: Implications for controls on the distribution of surface strain. Geophys. Res. Lett. 43, 10,115-10,124. https://doi.org/10.1002/2016GL069841

Mitchell, B.J., 1995. Anelastic structure and evolution of the continental crust and upper mantle from seismic surface wave attenuation. Rev. Geophys. 33, 441–462. https://doi.org/10.1029/95RG02074

Morelan, A.E. and Hernandez, J.L., 2020. Increasing Postearthquake Field Mapping Efficiency with Optical Image Correlation. *Bulletin of the Seismological Society of America*. 1–8, doi: 10.1785/0120200034

Murthy, K., Shearn, M., Smiley, B.D., Chau, A.H., Levine, J. and Robinson, M.D., 2014, October. SkySat-1: very high-resolution imagery from a small satellite. In *Sensors, Systems, and Next-Generation Satellites XVIII* (Vol. 9241, p. 92411E). International Society for Optics and Photonics.

Oskin, M., Perg, L., Shelef, E., Strane, M., Gurney, E., Singer, B., Zhang, X., 2008. Elevated shear zone loading rate during an earthquake cluster in eastern California. Geology 36, 507–510. https://doi.org/10.1130/G24814A.1

Oskin, M. and Iriondo, A., 2004. Large-magnitude transient strain accumulation on the Blackwater fault, Eastern California shear zone. *Geology*, *32*(4), pp.313-316. doi.org/10.1130/G20223.1

Ozacar, A.A., Beck, S.L., 2004. The 2002 Denali Fault and 2001 Kunlun Fault Earthquakes: Complex Rupture Processes of Two Large Strike-Slip Events. Bull. Seismol. Soc. Am. 94, S278–S292. https://doi.org/10.1785/0120040604

Petersen, M.D., Dawson, T.E., Chen, R., Cao, T., Wills, C.J., Schwartz, D.P., Frankel, A.D., 2011. Fault Displacement Hazard for Strike-Slip Faults Displacement Hazard for Strike-Slip Faults. Bull. Seismol. Soc. Am. 101, 805–825. https://doi.org/10.1785/0120100035

Peyrat, S., Olsen, K., Madariaga, R., 2001. Dynamic modeling of the 1992 Landers earthquake. J. Geophys. Res. Solid Earth 106, 26467–26482. https://doi.org/10.1029/2001JB000205

Platt J. Persistent slip rate discrepancies in the eastern California (USA) shear zone: Comment. Geology. 2017 Sep 1;45(9):e425-.

Platt, J.P., Becker, T.W., 2013. Kinematics of rotating panels of E–W faults in the San Andreas system: what can we tell from geodesy? Geophys. J. Int. 194, 1295–1301. https://doi.org/10.1093/gji/ggt189

Ponti, D.J., Blair, J.L., Rosa, C.M., K, T., Pickering, A.J., Morelan, A., Dawson, T., 2019. Digital datasets documenting surface fault rupture and ground deformation features produced by the Ridgecrest M6.4 and M7.1 earthquake sequence of July 4 and 5, 2019. US Geol. Surv. Data Release. https://doi.org/10.5066/P9BZ5IJ9

Ramsay, J.G., 1967. Folding And Fracturing Of Rocks. McGraw-Hill Book Company, New York p. 568.

Rice, J.R., 1975. On the stability of dilatant hardening for saturated rock masses. J. Geophys. Res. 1896-1977 80, 1531–1536. https://doi.org/10.1029/JB080i011p01531

Rockwell, T.K., Lindvall, S., Dawson, T., Langridge, R., Lettis, W., Klinger, Y., 2002. Lateral Offsets on Surveyed Cultural Features Resulting from the 1999 İzmit and Düzce Earthquakes, Turkey. Bull. Seismol. Soc. Am. 92, 79–94. https://doi.org/10.1785/0120000809

Rockwell, T.K., Lindvall, S., Herzberg, M., Murbach, D., Dawson, T., Berger, G., 2000. Paleoseismology of the Johnson Valley, Kickapoo, and Homestead Valley Faults: Clustering of Earthquakes in the Eastern California Shear Zone. Bull. Seismol. Soc. Am. 90, 1200–1236. https://doi.org/10.1785/0119990023

Ron, H., Freund, R., Garfunkel, Z., Nur, A., 1984. Block rotation by strike-slip faulting: Structural and paleomagnetic evidence. J. Geophys. Res. Solid Earth 89, 6256–6270. https://doi.org/10.1029/JB089iB07p06256

Ross, Z.E., Idini, B., Jia, Z., Stephenson, O.L., Zhong, M., Wang, X., Zhan, Z., Simons, M., Fielding, E.J., Yun, S.-H., Hauksson, E., Moore, A.W., Liu, Z., Jung, J., 2019.

Hierarchical interlocked orthogonal faulting in the 2019 Ridgecrest earthquake sequence. Science 366, 346–351. https://doi.org/10.1126/science.aaz0109

Sammis, C.G., Rosakis, A.J., Bhat, H.S., 2010. Effects of Off-fault Damage on Earthquake Rupture Propagation: Experimental Studies, in: Ben-Zion, Y., Sammis, C. (Eds.), Mechanics, Structure and Evolution of Fault Zones, Pageoph Topical Volumes. Birkhäuser, Basel, pp. 1629–1648. https://doi.org/10.1007/978-3-0346-0138-2_5

Savage, J.C., Burford, R.O., 1973. Geodetic determination of relative plate motion in central California. J. Geophys. Res. 1896-1977 78, 832–845. https://doi.org/10.1029/JB078i005p00832

Savage, J.C., Gan, W., Svarc, J.L., 2001. Strain accumulation and rotation in the Eastern California Shear Zone. J. Geophys. Res. Solid Earth 106, 21995–22007. https://doi.org/10.1029/2000JB000127

Savage, J.C., Svarc, J.L. and Prescott, W.H., 2004. Interseismic strain and rotation rates in the northeast Mojave domain, eastern California. *Journal of Geophysical Research: Solid Earth*, *109*(B2). https://doi.org/10.1029/2003JB002705

Scharer, K.M., Salisbury, J.B., Arrowsmith, J.R., Rockwell, T.K., 2014. Southern San Andreas Fault Evaluation Field Activity: Approaches to Measuring Small Geomorphic Offsets—Challenges and Recommendations for Active Fault Studies. Seismol. Res. Lett. 85, 68–76. https://doi.org/10.1785/0220130108

Schermer, E.R., Luyendyk, B.P. and Cisowski, S., 1996. Late Cenozoic structure and tectonics of the northern Mojave Desert. *Tectonics*, *15*(5), pp.905-932.

Scholz, C.H., 2019. *The mechanics of earthquakes and faulting*. Cambridge university press.

Scott, C.P., Arrowsmith, J.R., Nissen, E., Lajoie, L., Maruyama, T., Chiba, T., 2018. The M7 2016 Kumamoto, Japan, Earthquake: 3-D Deformation Along the Fault and Within the Damage Zone Constrained From Differential Lidar Topography. J. Geophys. Res. Solid Earth 123, 6138–6155. https://doi.org/10.1029/2018JB015581

Shelef, E., Oskin, M., 2010. Deformation processes adjacent to active faults: Examples from eastern California. J. Geophys. Res. Solid Earth 115. https://doi.org/10.1029/2009JB006289

Shi Z, Day SM., 2013, Rupture dynamics and ground motion from 3-D rough-fault simulations. Journal of Geophysical Research: Solid Earth. Mar;118(3):1122-41.

Sieh, K., Jones, L., Hauksson, E., Hudnut, K., Eberhart-Phillips, D., Heaton, T., Hough, S., Hutton, K., Kanamori, H., Lilje, A. and Lindvall, S., 1993. Near-field investigations of the Landers earthquake sequence, April to July 1992. Science, 260(5105), pp.171-176.

Smith, K., Hatch, R. L., Ruhl, C. J., & Abercrombie, R. E. (2020, 08). Order and timing of high-angle conjugate strike-slip faulting in Walker Lane sequences. Poster Presentation at 2020 SCEC Annual Meeting.

Socquet, A., Hollingsworth, J., Pathier, E., Bouchon, M., 2019. Evidence of supershear during the 2018 magnitude 7.5 Palu earthquake from space geodesy. Nat. Geosci. 12, 192–199. https://doi.org/10.1038/s41561-018-0296-0

Stirling MW, Wesnousky SG, Shimazaki K. Fault trace complexity, cumulative slip, and the shape of the magnitude-frequency distribution for strike-slip faults: A global survey. Geophysical Journal International. 1996 Mar 1;124(3):833-68.

Tchalenko JS. Similarities between shear zones of different magnitudes. Geological Society of America Bulletin. 1970 Jun 1;81(6):1625-40.

Teran, O.J., Fletcher, J.M., Oskin, M.E., Rockwell, T.K., Hudnut, K.W., Spelz, R.M., Akciz, S.O., Hernandez-Flores, A.P., Morelan, A.E., 2015. Geologic and structural controls on rupture zone fabric: A field-based study of the 2010 Mw 7.2 El Mayor–Cucapah earthquake surface rupture. Geosphere 11, 899–920. https://doi.org/10.1130/GES01078.1

Thomas, M.Y., Bhat, H.S., 2018. Dynamic evolution of off-fault medium during an earthquake: a micromechanics based model. Geophys. J. Int. 214, 1267–1280. https://doi.org/10.1093/gji/ggy129

U.S. Geological Survey and California Geological Survey, Quaternary fault and fold database for the United States, accessed March 1 2020, at: https://www.usgs.gov/natural-hazards/earthquake-hazards/faults.

Vidale JE, Li YG. Damage to the shallow Landers fault from the nearby Hector Mine earthquake. 2003, Nature Jan;421(6922):524-6.

Wang, K., Dreger, D. S., Tinti, E., Bürgmann, R., and Taira, T., 2020, Rupture process of the 2019 Ridgecrest, California M6.4 Foreshock and M7.1 Earthquake Constrained by Seismic and Geodetic Data, Bull. Seismol. Soc. Am. 92, https://doi.org/10.1785/0120200108

Wesnousky, S.G., 1988. Seismological and structural evolution of strike-slip faults. *Nature*, *335*(6188), pp.340-343.

Wesnousky, S.G., 2005. The San Andreas and Walker Lane fault systems, western North America: transpression, transtension, cumulative slip and the structural evolution of a major transform plate boundary. J. Struct. Geol. 27, 1505–1512. https://doi.org/10.1016/j.jsg.2005.01.015

Willis, MJ; Barnhart, WD; Cassotto, R; Klassen, J; Corcoran, J; Host, T; Huberty, B., Pelletier, K., Knight, J.F., *CaliDEM: Ridgecrest, CA Region 2m Digital Surface Elevation Model.* Funding by NSF and USGS. Data collection by DigitalGlobe. Distributed by OpenTopography. https://doi.org/10.5069/G998854C

Xu, X., Sandwell, D.T., Smith-Konter, B., 2020. Coseismic Displacements and Surface Fractures from Sentinel-1 InSAR: 2019 Ridgecrest Earthquakes. Seismol. Res. Lett. https://doi.org/10.1785/0220190275

Xu, X., Tong, X., Sandwell, D.T., Milliner, C.W.D., Dolan, J.F., Hollingsworth, J., Leprince, S., Ayoub, F., 2016. Refining the shallow slip deficit. Geophys. J. Int. 204, 1867–1886. https://doi.org/10.1093/gji/ggv563

Zinke, R., Hollingsworth, J. and Dolan, J.F., 2014. Surface slip and off-fault deformation patterns in the 2013 MW 7.7 B alochistan, Pakistan earthquake: Implications for controls on the distribution of near-surface coseismic slip. *Geochemistry, Geophysics, Geosystems*, *15*(12), pp.5034-5050.

Zhou, Y., Parsons, B.E., Walker, R.T., 2018. Characterizing Complex Surface Ruptures in the 2013 Mw 7.7 Balochistan Earthquake Using Three-Dimensional Displacements. J. Geophys. Res. Solid Earth 123, 10,191-10,211. https://doi.org/10.1029/2018JB016043

Table 1 Summary of statistics and values estimated for the foreshock fault rupture that includes comparisons of observed and predicted values for the bookshelf slip model.

	Observed	**Predicted**
Dextral slip (γ, meter)	0.98	-
Angle between faults (α, º)	86	-

Sinistral slip (γ', meter)	0.71−1.4	0.97
Cumulative displacement (*d_{fore}*)	256-600	-
Total long-term block rotation (ω_T, º)	3-7	-
Mean displacement ($\bar{d}$, meter)	0.71	-
Maximum displacement, (meter)	1.4	-
Median off-fault deformation (OFD, %)	65	-
Mean off-fault deformation (OFD, %)	56	-
Mean Fault zone width	59	-
Shallow slip deficit (%)	42-65*	-

*(*Chen et al., 2020; Jin & Fialko, 2020; Wang et al., 2020; Xu et al., 2020*)

Table 2 Summary of statistics and values estimated for the mainshock fault rupture that includes comparison of observed and predicted values for the bookshelf slip model.

	Observed	**Predicted**
Dextral slip (γ, meter)	1.6	-
Angle between faults (α, º)	66	-
Sinistral slip (γ', meter)	0.8	1
Instantaneous block rotation (ω, º)	0.06	0.05
Internal block strain (e, %)	0.004	0.0044
Mean displacement ($\bar{d}$, meter)	1.69	-
Macroscopic block width (w_b, meter)	4,890	
Median off-fault deformation (OFD, %)	25	-
Mean off-fault deformation (OFD, %)	34	-
Mean Fault zone width (fault-zone width, meter)	69	-
Shallow slip deficit (%)	18-35*	-

*(Chen et al., 2020; Jin & Fialko, 2020; Wang et al., 2020; Xu et al., 2020)

Figures

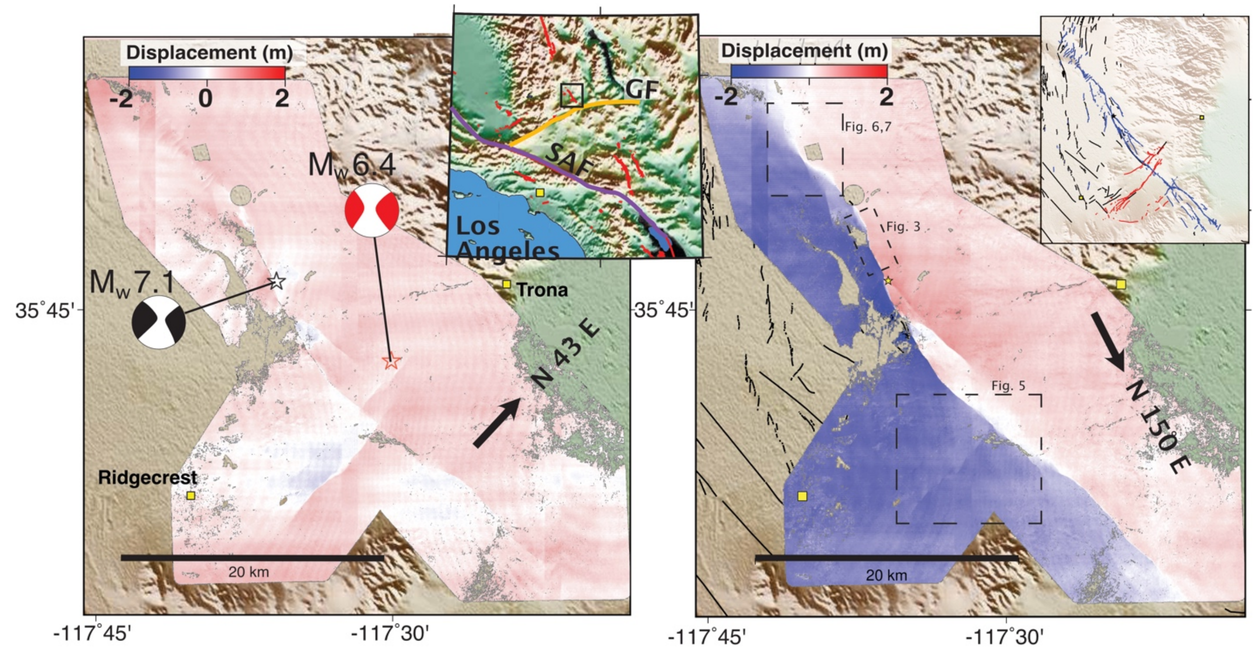

Figure 1. Displacement maps from optical image correlation that measures surface motion from both the foreshock (July 4th, 2019) and mainshock ruptures (July 6th, 2019). The pre-event image was acquired on September 15th, 2018 and the post image on July 24th, 2019 and therefore surface motion from both events are found within the surface displacement maps. A) Displacement projected into the N43ºE direction parallel to foreshock faults. Inset shows the location of Ridgecrest region (black rectangle), San Andreas fault (SAF, purple line) and Garlock fault (GF, orange line). B) Displacement projected into the N150ºE direction, parallel to mainshock faults. Focal mechanisms from CMT catalogue. (Dziewonski et al., 1981; Ekström et al., 2012). Inset in upper right shows fault rupture traces of the foreshock (red) and mainshock (blue) mapped from field surveys (Ponti et al., 2020), with black lines showing Quaternary mapped faults (USGS, 2020).

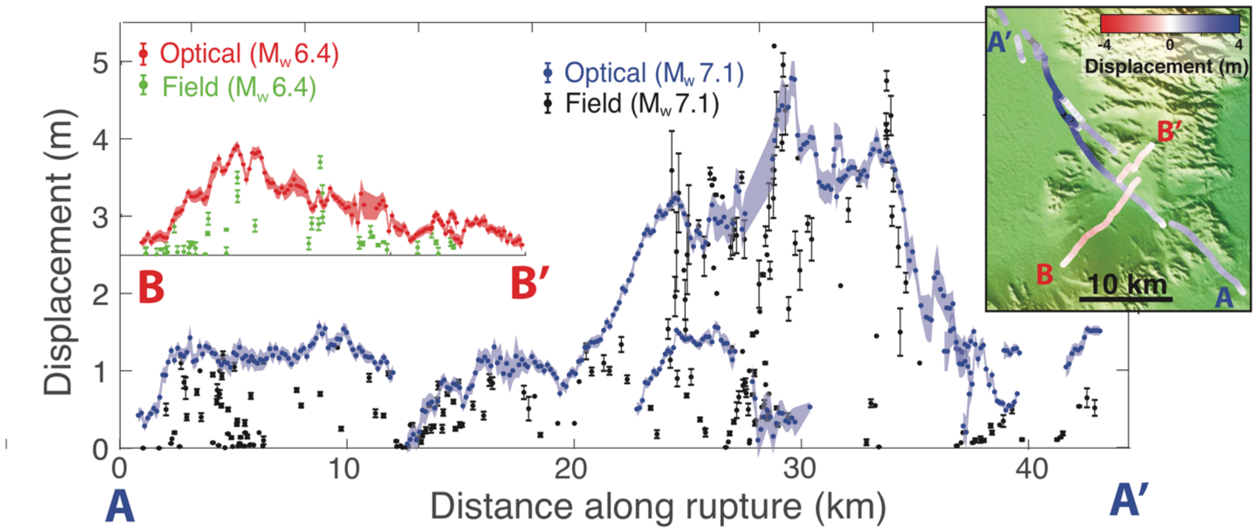

Figure 2. Comparison of slip profiles of the foreshock and mainshock events made from field and optical measurements. Slip along the foreshock is measured along three parallel fault strands and slip along the mainshock is measured along eight. Red and green values show optical and field measurements along the foreshock rupture, respectively, and blue and black are optical and field measurements along the mainshock, respectively. Optical displacements capture the total displacement across the surface rupture using profiles with > 0.5 km in across-fault length (e.g., Figure S1), which includes both on-fault displacement and off-fault distributed inelastic strain, explaining why the majority are larger than the field displacement measurements from Ponti et al. (2019). Inset in top right shows the same optical displacement measurements in map view.

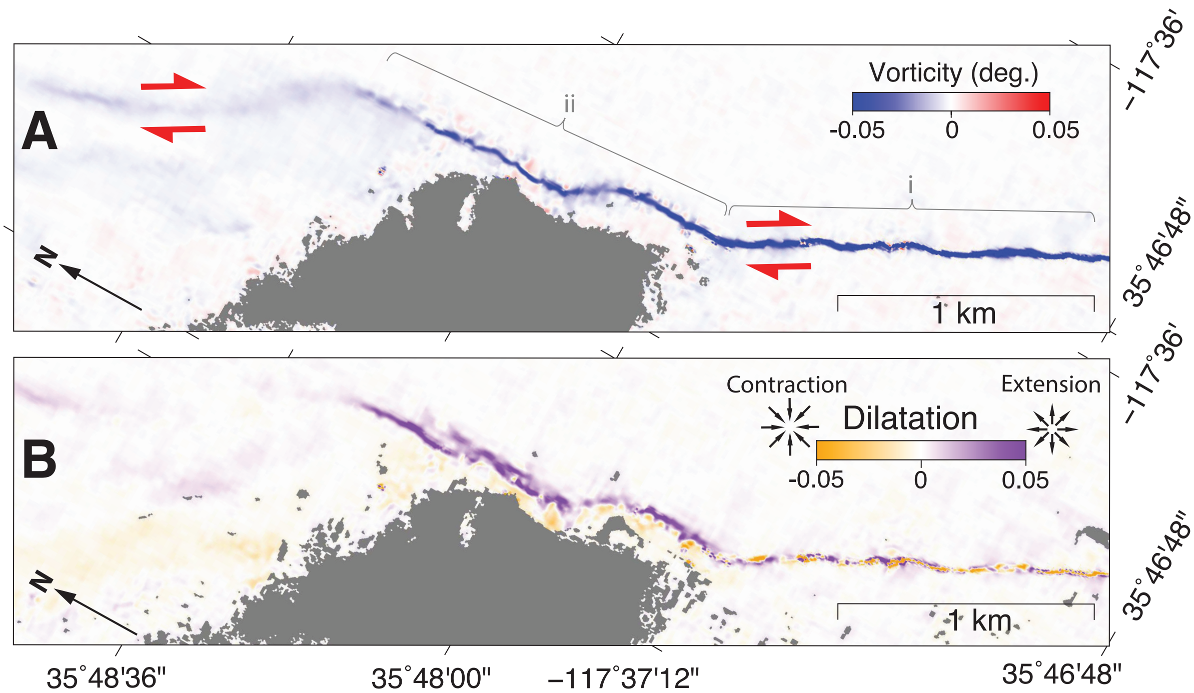

Figure 3. Strain maps along a transtensional bend. A) Vorticity along a transtensional bend located near the northern end of the mainshock rupture (see Figure 1 for location), segments i and ii show location of profiles used in Fig. 4b and c. B) Dilatational strain component along the transtensional bend showing systematic variations of width between the bend and adjacent linear segment, and variations of the type of dilatation according to subtle curvature of the fault along segment i. See Figure 1 for locations.

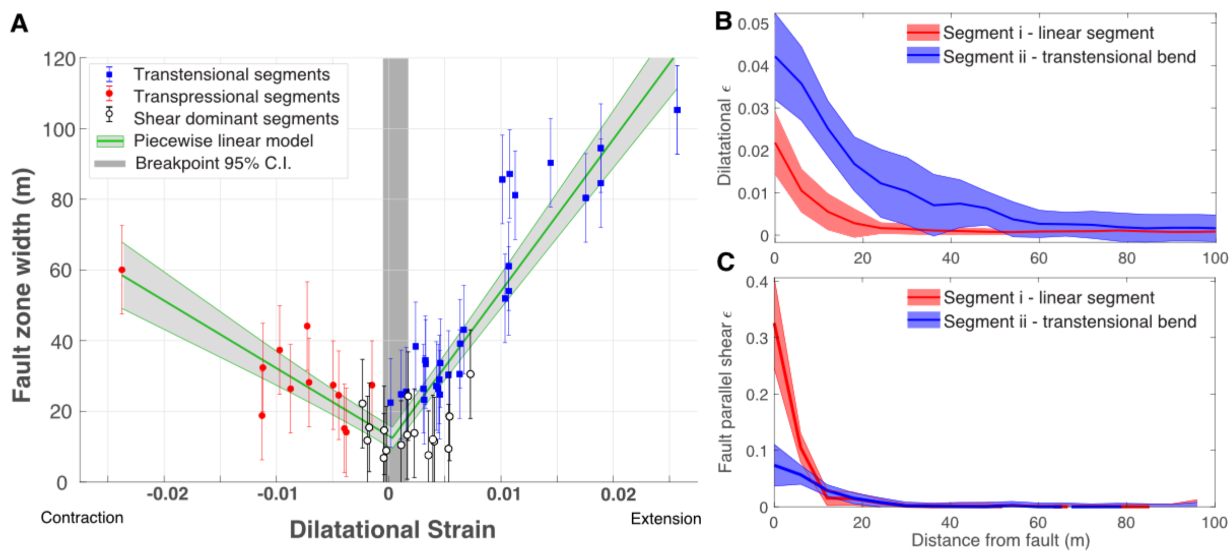

Figure 4. Variation of fault zone width with dilatational strain. A) Fault width measured from three different strain regimes, contractional (red), shear dominated (white), and extensional (blue), which shows a segmented piecewise linear function can explain the variation, with wider fault zones with increasing amounts of dilatational strain. Dark vertical gray band is 95% confidence interval of the breakpoint estimated by bootstrapping the data with 3000 simulations. Light gray bands are 95% confidence intervals of the segmented regression. B) shows dissipation of inelastic strain from strain profiles taken across the transtensional bend (segment ii) from the dilatation map shown in Fig. 3c, where dilatational strain is significantly wider along transtensional bend than adjacent segment (segment i) that experiences mostly shear strain. C) shows fault-parallel shear strain, with high-strain fault core along segment i and lower shear strains in ii.

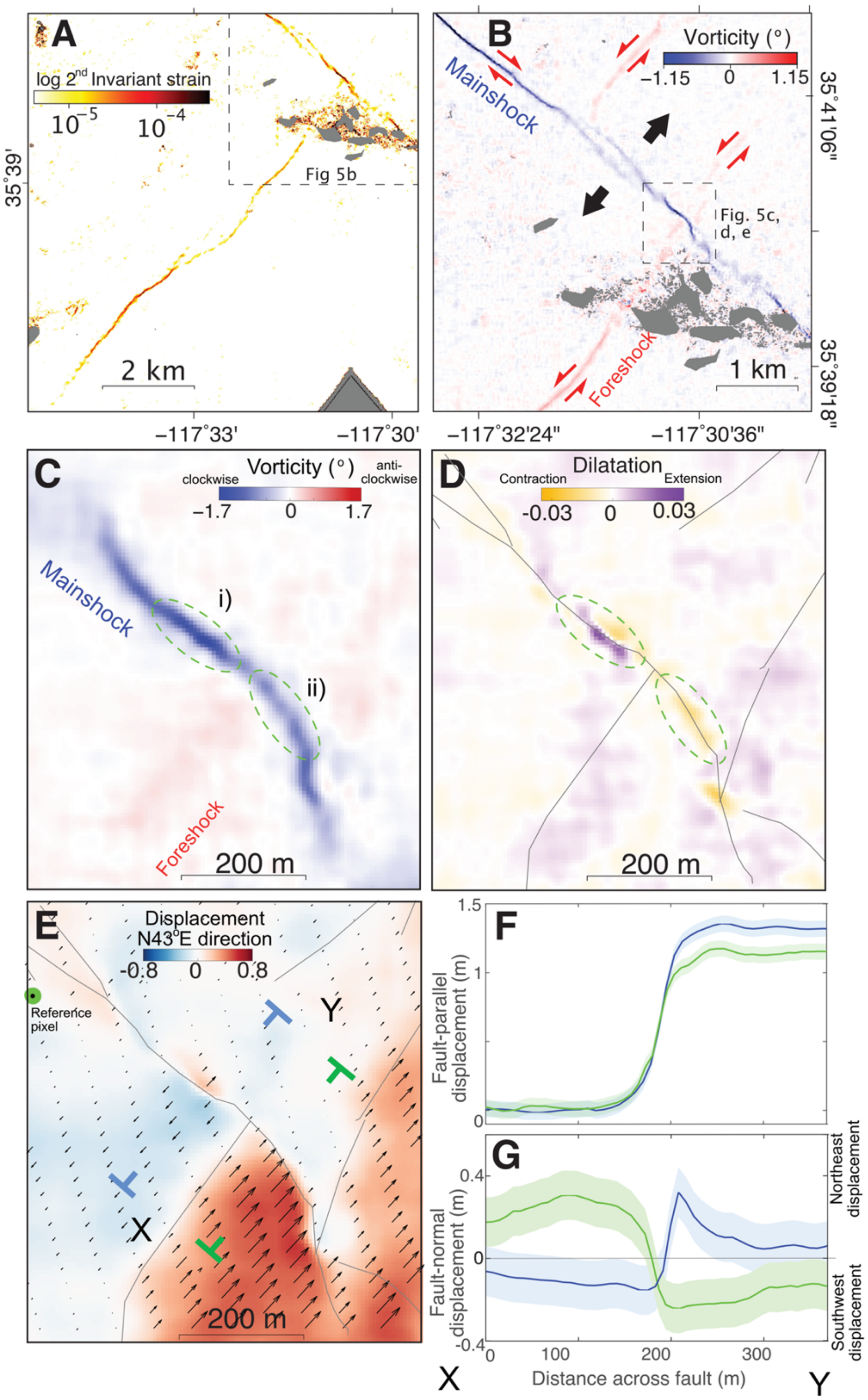

Figure 5. Strain maps of the foreshock-mainshock intersection region illustrating how strain release along the mainshock was affected by the foreshock rupture. a) Logarithm of I_2, which illustrates how the scalar strain intensity varies along the rupture. b) Vorticity map illustrating the different shear senses around the mainshock-foreshock intersection. c) Zoom of vorticity map illustrating an increase along segment i) and lower values along segment ii), suggesting a possible

difference in the intensity of simple shear strain. d) Dilatation of the intersection region highlighting how different segments experienced contraction (orange) and extension (purple) due to imposed stress changes from the foreshock rupture. Gray lines show major fault traces from field mapping (Ponti et al., 2020). e) Surface displacement projected into the NE direction, illustrating motion perpendicular to the mainshock rupture shown both by the colors (amplitude of motion) and the vectors. This shows clear extension across the blue profile (vectors diverging away from each across the mainshock rupture) and contraction across the green profile (shown by vectors converging across the mainshock rupture, profiles labelled X-Y), which are plotted in f) and g).

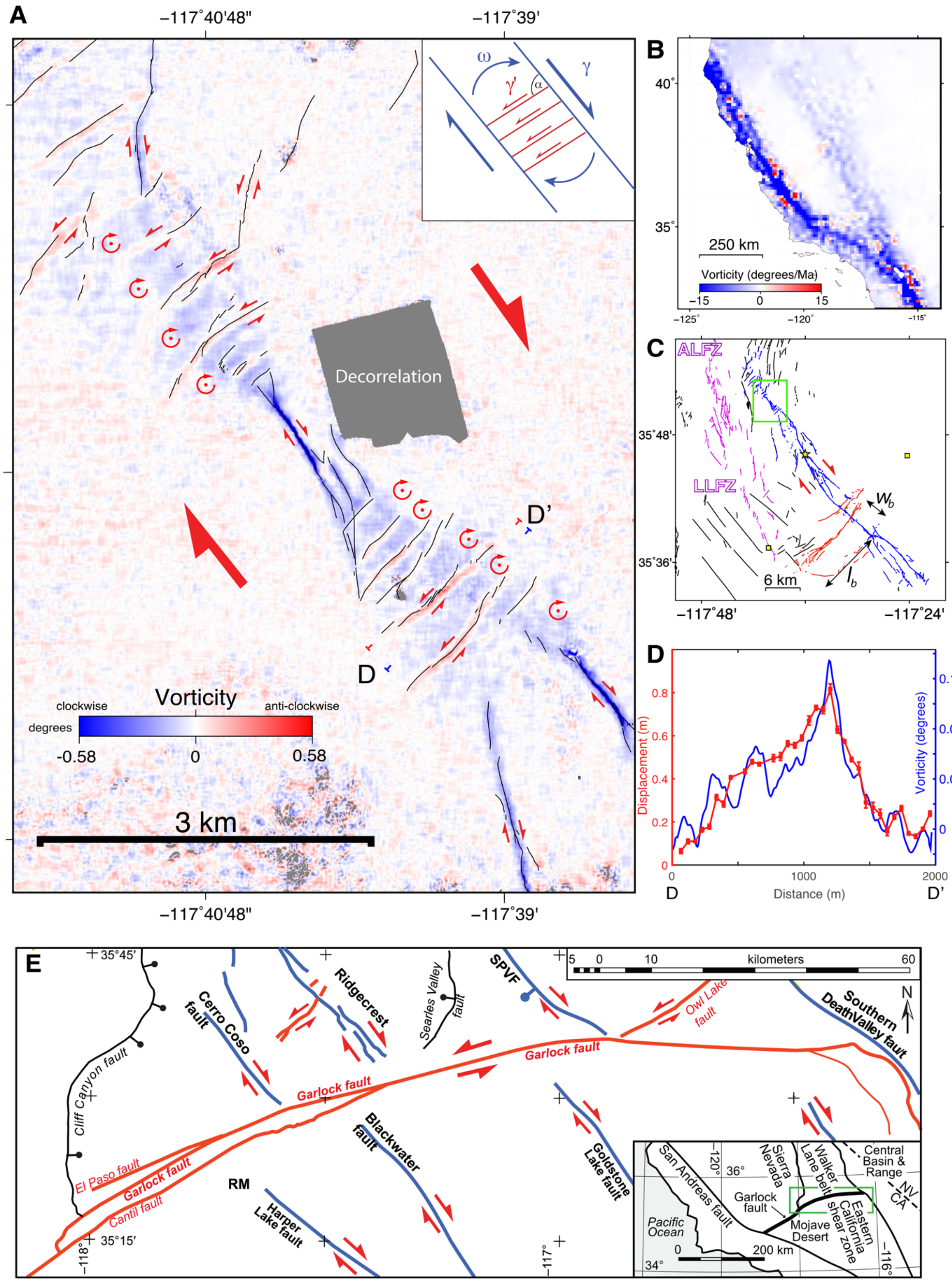
A
−117°40'48"
−117°39'
35°52'48"
35°51'
35°49'12"
Decorrelation
D'
D
Vorticity
clockwise
anti-clockwise
degrees
-0.58
0
0.58
3 km
ω
γ
γ'
α
B
40°
35°
250 km
Vorticity (degrees/Ma)
−15
0
15
−125°
−120°
−115°
C
ALFZ
LLFZ
35°48'
35°36'
6 km
W_b
l_b
−117°48'
−117°24'
D
Displacement (m)
Vorticity (degrees)
Distance (m)
0
1000
2000
0.8
0.6
0.4
0.2
0.12
0.08
0.04
E
35°45'
35°15'
−118°
−117°
Cliff Canyon fault
Cerro Coso fault
Ridgecrest
Searles Valley fault
SPVF
Owl Lake fault
Southern DeathValley fault
Garlock fault
El Paso fault
Cantil fault
Blackwater fault
Goldstone Lake fault
Harper Lake fault
RM
kilometers
5
0
10
60
N
San Andreas fault
Sierra Nevada
Walker Lane belt
Central Basin & Range
NV
CA
Garlock fault
Eastern California shear zone
Mojave Desert
Pacific Ocean
200 km
−120°
36°
34°
−116°

Figure 6. Vorticity of the vector field illustrating bookshelf faulting and rotations associated with simple shear. Location is shown as the green box in c) and Figure 1. A) Positive (negative) colors show anti-clockwise (clockwise) rotation in a right-handed coordinate system. Black lines are faults mapped in the field (Ponti et al., 2019). The vorticity illustrates that strain beyond the fault tips of dextral faults transition to rotation, where according to field mapping (black lines) fracturing is only limited to larger, finite amounts of strain, suggesting rotation accommodates lower strains between faults. Inset shows schematic illustrating the kinematics of bookshelf slip model consisting of regional dextral displacement (blue lines, γ), rotation of blocks (ω), rotation of sinistral oblique fault (α), and slip on oblique faults (red, γ'), modified from Platt & Becker (2013). B) Vorticity rate from GPS velocities along the North America-Pacific plate boundary, blue is clockwise, red anticlockwise from Kremeer et al. (2014). C) Fault traces of the foreshock rupture (red), mainshock (blue) and Little Lake and Airport Fault Zones (LLFZ, ALFZ, magenta), illustrating the larger scale 'bookshelf' with block width (w_b). D) Profile of vorticity and displacement along and adjacent to the second southernmost sinistral fault (note displacement is measured from displacement map shown in Fig. 6b), where a non-constant vorticity and slip is evidence of non-rigid block strain. E) Map view of NW-trending dextral faults of the ECSZ show that they do not intersect with the sinistral WSW-trending Garlock fault, which could be explained by clockwise block rotation beyond the tips of dextral faults similar to that found in a), figure adapted from Andrew et al. (2015).

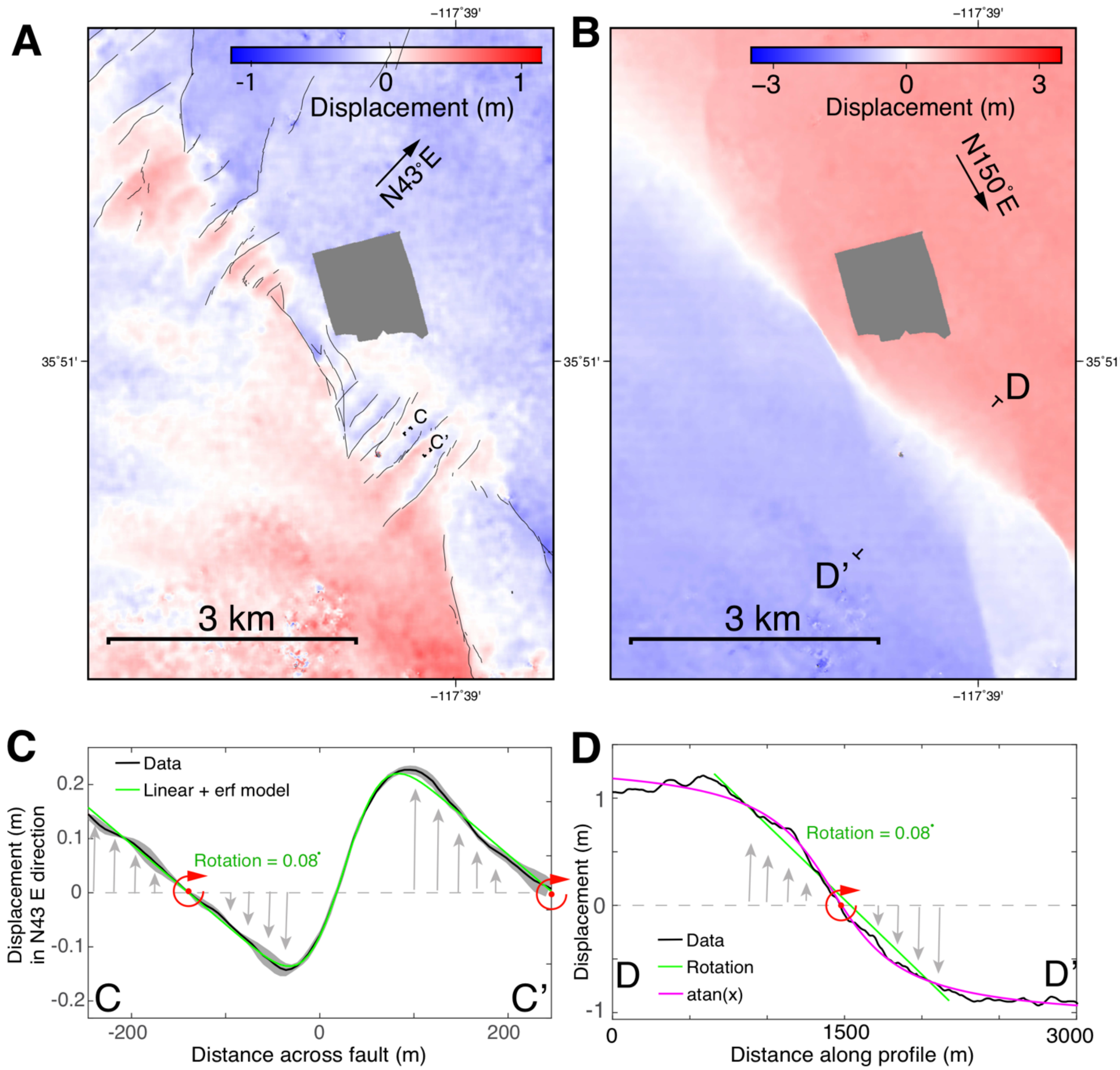

Figure 7. Projected surface displacement illustrating bookshelf kinematics. Location shown in Figure 1. A) shows displacement projected into NE that highlights motion along the oblique NE trending sinistral faults and contraction of dextral faults, while b) shows displacement projected into SE direction parallel to the NW-trending dextral faults illustrating distributed shear across the bookshelf. C) shows profile of displacement from a) normal to one of the sinistral oblique faults illustrating rotation of displacement discontinuities (location is shown in panel A between the labels C-C'). D) shows that distributed shear across the bookshelf is not well explained by constant motion (green line) indicative of rigid-block rotation, but instead by shear that increases towards the center of the 'bookshelf' described by an arctan function from a screw dislocation model (location of profile is shown in b), between labels D and D'). Inverting the surface motion (black

line) suggests a possible single, freely slipping, discrete fault that reaches from depth to 342 m below the surface (magenta line).

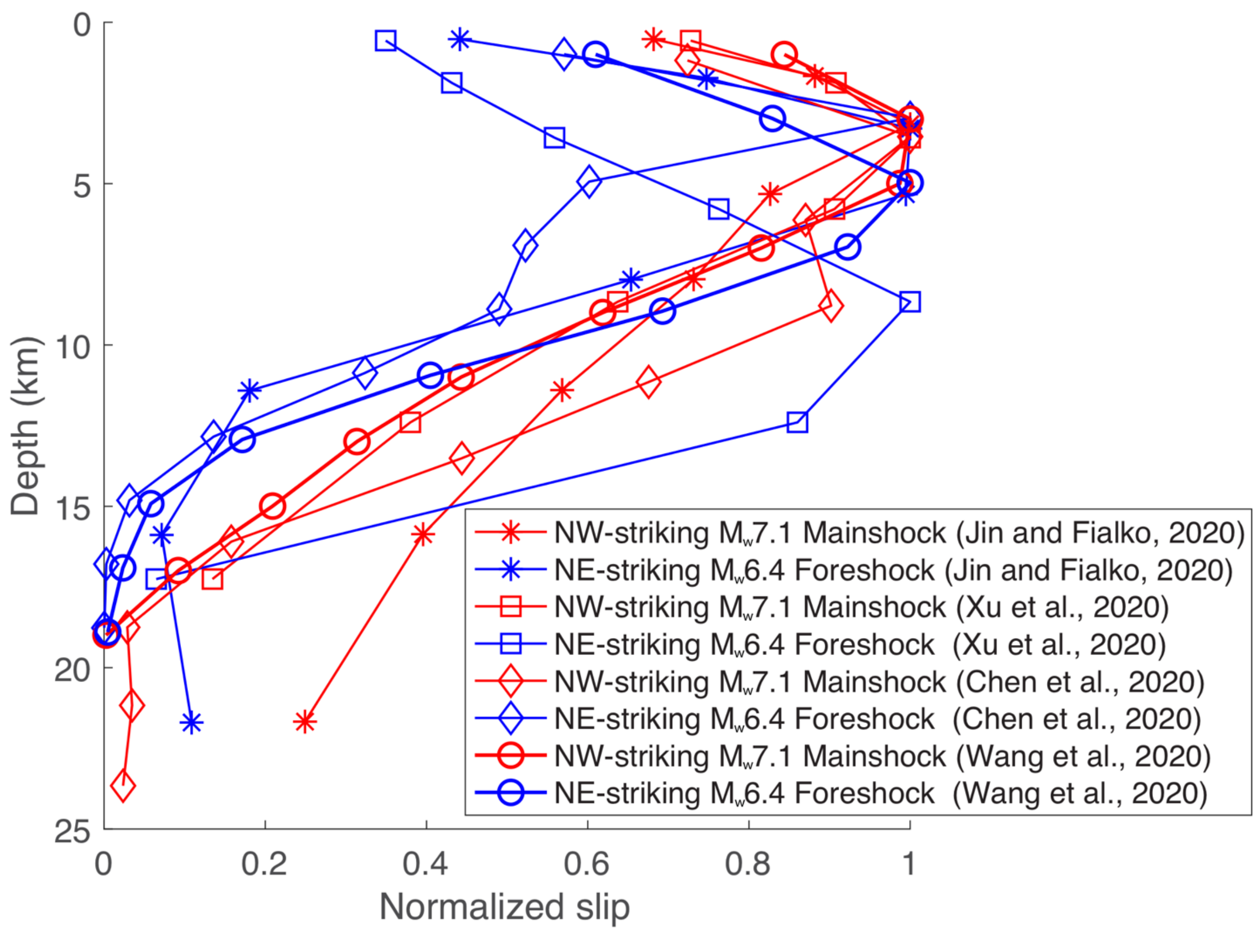

Figure 8. Normalized slip depth distributions for the M_w 6.4 foreshock (blue) and the M_w 7.1 mainshock (red) from different slip inversions. Here we have assumed that the M_w 6.4 foreshock rupture was mainly along the NE-striking sinistral fault segments, whereas the M_w 7.1 mainshock rupture was along the NW-striking dextral faults, although seismicity and inversion of seismic and geodetic data suggest that the M_w 6.4 foreshock may involve rupturing along the NW-striking faults too (Ross et al., 2019; Chen et al., 2020; Wang et al., 2020). Despite large variations among these models they all systematically show that the foreshock had a higher shallow slip deficit ranging from 42-65% while the mainshock ranges from 18-35% (Chen et al., 2020; Jin and Fialko, 2020; Wang et al., 2020; Xu et al., 2020).